

## ALMA 200-PARSEC RESOLUTION IMAGING OF SMOOTH COLD DUSTY DISKS IN TYPICAL $z \sim 3$ STAR-FORMING GALAXIES

W. RUJOPAKARN<sup>1,2,3</sup>, E. DADDI<sup>4</sup>, G. H. RIEKE<sup>5</sup>, A. PUGLISI<sup>4</sup>, M. SCHRAMM<sup>6</sup>, P. G. PÉREZ-GONZÁLEZ<sup>7</sup>,  
G. E. MAGDIS<sup>8,9</sup>, S. ALBERTS<sup>5</sup>, F. BOURNAUD<sup>4</sup>, D. ELBAZ<sup>4</sup>, M. FRANCO<sup>4</sup>, R. J. IVisON<sup>10,11</sup>, L. KAWINWANICHAKIJ<sup>3</sup>,  
K. KOHNO<sup>12,13</sup>, D. NARAYANAN<sup>8,14,15</sup>, J. D. SILVERMAN<sup>3</sup>, T. WANG<sup>6,12,13</sup>, AND C. C. WILLIAMS<sup>5</sup>

<sup>1</sup>Department of Physics, Faculty of Science, Chulalongkorn University, 254 Phayathai Road, Pathumwan, Bangkok 10330, Thailand

<sup>2</sup>National Astronomical Research Institute of Thailand (Public Organization), Don Kaeo, Mae Rim, Chiang Mai 50180, Thailand

<sup>3</sup>Kavli IPMU (WPI), UTIAS, The University of Tokyo, Kashiwa, Chiba 277-8583, Japan; wiphu.rujopakarn@ipmu.jp

<sup>4</sup>CEA, IRFU, DAp, AIM, Université Paris-Saclay, Université de Paris, Sorbonne Paris Cité, CNRS, F-91191 Gif-sur-Yvette, France

<sup>5</sup>Steward Observatory, The University of Arizona, Tucson, AZ 85721, USA

<sup>6</sup>National Astronomical Observatory of Japan, Mitaka, Tokyo, 181-8588, Japan

<sup>7</sup>Centro de Astrobiología (CAB, CSIC-INTA), Carretera de Ajalvir km 4, E-28850 Torrejón de Ardoz, Madrid, Spain

<sup>8</sup>Cosmic Dawn Center, Niels Bohr Institute, University of Copenhagen, Juliane Mariesvej 30, 2100, Copenhagen, Denmark

<sup>9</sup>Institute for Astronomy, Astrophysics, Space Applications and Remote Sensing, National Observatory of Athens, 15236, Athens, Greece

<sup>10</sup>European Southern Observatory, Karl Schwarzschild Strasse 2, Garching, Germany

<sup>11</sup>Institute for Astronomy, University of Edinburgh, Blackford Hill, Edinburgh EH9 3HJ, UK

<sup>12</sup>Institute of Astronomy, The University of Tokyo, Osawa, Mitaka, Tokyo 181-0015, Japan

<sup>13</sup>Research Center for the Early Universe, The University of Tokyo, 7-3-1 Hongo, Bunkyo-ku, Tokyo 113-0033, Japan

<sup>14</sup>Department of Astronomy, University of Florida, 211 Bryant Space Sciences Center, Gainesville, FL 32611 USA

<sup>15</sup>University of Florida Informatics Institute, 432 Newell Drive, CISE Bldg E251, Gainesville, FL 32611, USA

Draft version June 25, 2022

### ABSTRACT

We present high-fidelity, 30 milliarcsecond (200-pc) resolution ALMA rest-frame 240  $\mu\text{m}$  observations of cold dust emission in three typical  $z \sim 3$  star-forming galaxies in the Hubble Ultra-Deep Field (HUDF). The cold dust is distributed within the smooth disk-like central regions of star formation (SF) 1 – 3 kpc in diameter, despite their complex and disturbed rest-frame UV and optical morphologies. No dust substructures or clumps are seen down to  $\simeq 1 - 3 M_{\odot}\text{yr}^{-1}$  ( $1\sigma$ ) per 200-pc beam. No dust emission is observed at the locations of UV-emitting clumps, which lie  $\simeq 2 - 10$  kpc from the bulk of SF. Clumpy substructures can contribute no more than 1 – 8% ( $3\sigma$  upper limits) of the total SF in these galaxies. The lack of SF substructures in our HUDF galaxies is to be contrasted with the multiple substructures characteristic of submillimeter-selected galaxies (SMGs) at the same cosmic epoch, each containing  $\sim 10 - 30\%$  of their total SF. We find that individual substructures of SMGs are often as bright in the far-infrared as (or in some cases brighter than) our HUDF galaxies, suggesting that these SMGs originate from a class of disruptive event involving multiple objects at the scale of our HUDF galaxies. The scale of the disruptive event found in our HUDF galaxies, characterized by the lack of star-forming substructures at our resolution and sensitivity, could be less violent, e.g., gas-rich disk instability or minor mergers.

*Subject headings:* galaxies: evolution — galaxies: formation — galaxies: star formation — galaxies: structure — galaxies: high-redshift

### 1. INTRODUCTION

A key achievement in the past two decades has been the progress in understanding the evolution of the *spatially-integrated* properties of galaxies across cosmic time. The cosmic histories of the star formation rate (SFR), stellar mass build up, and massive black hole accretion have been constrained out to the epoch of reionization (e.g. Madau & Dickinson 2014; Heckman & Best 2014; Grazian et al. 2015). With appropriate sets of parameters, models of galaxy evolution can reproduce these histories as well as the general properties of today’s galaxies (e.g. Behroozi et al. 2013; Somerville & Davé 2015; Schaye et al. 2015; Springel et al. 2018). However, many of the most fundamental processes are not well understood, especially down to *sub-galactic* scales, where pressing frontier questions in galaxy evolution lie: How did galactic spheroids form? How did galaxies and their supermassive black holes co-evolve?

There is a broad consensus that galaxies assemble most of their stellar mass via accretion of cold gas, which leads

to gas-rich, unstable disks and in-situ disk-wide star formation (‘cold mode’ accretion; Noguchi 1999; Immeli et al. 2004; Kereš et al. 2005; Bournaud et al. 2007; Dekel et al. 2009; Ceverino et al. 2010; Inoue et al. 2016). Multiple lines of evidence support this consensus, such as the relationship between star formation and stellar mass at  $z \sim 0 - 6$  (the ‘main sequence’, e.g., Brinchmann et al. 2004; Noeske et al. 2007; Salim et al. 2007; Wuyts et al. 2011; Whitaker et al. 2012; Speagle et al. 2014; Salmon et al. 2015) and the rarity of compact starbursts at  $z \sim 2$  as indicated by the distribution of specific star-formation rates (sSFR) and of the infrared colors (Rodighiero et al. 2011; Elbaz et al. 2011). Observations of individual  $z \sim 1 - 3$  galaxies provide further support. Spatially-resolved kinematic observations showed that typical star-forming galaxies (defined here as those with specific star formation rates of a few  $\text{Gyr}^{-1}$ , i.e., on the main sequence; hereafter ‘typical SFGs’) are isolated (i.e., not undergoing major mergers), rotation-dominated systems (e.g., Förster Schreiber et al. 2009; Wisnioski et al. 2015;

Stott et al. 2016). Dust-independent, sub-arcsecond radio continuum imaging and stacking further reveal that typical SFGs have intensely star-forming regions a few kpc in diameter (Lindroos et al. 2016; Rujopakarn et al. 2016), comparable to the typical sizes of massive galaxies at the same epoch, despite forming stars at rates only achievable in the local Universe in the compact nuclei of galaxy mergers (e.g., Muxlow et al. 2005; Rujopakarn et al. 2011). These observations suggest that we are on the right track toward understanding how typical massive galaxies were assembled.

A key prediction from simulations of star formation being fed by cold-mode accretion is the fragmentation of the disk and the emergence of star-forming clumps. The inward migration of these clumps is an integral part of the bulge formation scenario (e.g., Bournaud et al. 2007; Agertz et al. 2009; Dekel et al. 2009; Ceverino et al. 2010; Mandelker et al. 2014) and could be an intermediary regulating the bulge–SMBH relationship (Martig et al. 2009; Gabor & Bournaud 2013). Clumpy star formation in the formative era may also explain the bimodality in  $\alpha$ -abundance and metallicity ( $[\alpha/\text{Fe}]$  vs.  $[\text{Fe}/\text{H}]$ ) in the Milky Way (Clarke et al. 2019). To play a significant role in bulge and galaxy assembly, clumps have to survive radiative and mechanical feedback long enough to accrete fresh fuel and migrate; simulations disagree whether this is possible (for both sides of the argument, see, e.g., Genel et al. 2012; Bournaud et al. 2014).

When rest-frame UV images from the *Hubble Space Telescope* (*HST*) revealed irregular morphologies in  $z \sim 1 - 3$  galaxies, suggesting the detection of the predicted star-forming clumps, there was a flurry of studies in the context of bulge formation (Cowie et al. 1995; van den Bergh et al. 1996; Conselice 2003; Elmegreen & Elmegreen 2005). These UV-bright star-forming clumps are ubiquitous features in  $z \sim 1 - 3$  galaxies. They appear to be  $\sim 1$  kpc in size, contain  $10^8 - 10^9 M_\odot$  of stellar mass, form stars at  $1 - 30 M_\odot \text{yr}^{-1}$ , and reside in kinematically-ordered systems. Their size, mass, SFRs, and age gradients are broadly consistent with the clump-driven bulge formation scenario (Elmegreen et al. 2007; Bournaud et al. 2008; Genzel et al. 2008; Elmegreen et al. 2009a,b; Genzel et al. 2011; Förster Schreiber et al. 2011; Livermore et al. 2012; Wisnioski et al. 2012; Guo et al. 2012; Menéndez-Delmestre et al. 2013; Guo et al. 2015; Livermore et al. 2015; Soto et al. 2017; Guo et al. 2018). However, it has gradually become apparent that the UV clumps only contain  $\lesssim 5 - 20\%$  of the total star-formation in SFGs at  $z \sim 2$  (e.g., Wuyts et al. 2012; Soto et al. 2017; Guo et al. 2018). These clumps are conspicuously absent from deep sub-arcsecond Atacama Large Millimeter/submillimeter Array (ALMA) and Karl G. Jansky Very Large Array (VLA) images of massive main-sequence SFGs. Rujopakarn et al. (2016) showed that the UV-selected clumps are often peripheral to the central region of star formation, which is dust-obscured and can only be traced with extinction-independent imaging at longer wavelengths. Cibinel et al. (2017) conducted sensitive CO(5–4) observations of an archetypal clumpy galaxy UDF6462 (Bournaud et al. 2008) and found that no more than 3% of the total molecular gas in the galaxy can be in each clump, with most of the cold gas residing in the central star-forming region. That is, the UV-selected clumps do not appear to

be the dominant star-forming clumps predicted by theory. Either the predicted star-forming clumps reside in the heavily obscured region around the nuclei and close to the bulk of star formation, or our picture of clump-facilitated bulge assembly may need to be re-thought.

The central regions that dominate the star formation in typical massive SFGs at  $z \sim 2$  are  $\simeq 4 - 5$  kpc in diameter (Lindroos et al. 2016; Rujopakarn et al. 2016). Those of starburst galaxies (i.e., those with sSFR above the scatter of the main sequence) and sub/millimeter-selected galaxies (SMGs) are smaller,  $\simeq 1 - 2$  kpc in diameter (Simpson et al. 2015; Ikarashi et al. 2015). Even for typical massive SFGs, these regions are so dusty that all but  $\sim 1\%$  of the star formation is obscured in the UV (Dunlop et al. 2017). For SMGs very high obscuration,  $A_V \sim 100$  mag toward the center, is not uncommon (Simpson et al. 2017). Probing the structure of these regions requires an extinction-independent tracer of star formation that is capable of sub-kpc resolution. Major progress in dissecting these regions is being made by: (1) sub/millimeter observations of gravitationally lensed galaxies (often SMGs, e.g., ALMA Partnership et al. 2015; Swinbank et al. 2015; Tamura et al. 2015; Dye et al. 2015), and (2) exploiting the resolution and sensitivity of ALMA on field galaxies (e.g., Iono et al. 2016; Hodge et al. 2016; Oteo et al. 2017; Gullberg et al. 2018; Tadaki et al. 2018; Hodge et al. 2019).

For different reasons, both approaches often capture SFGs far more luminous than the typical population. First, the lens selection at sub/millimeter wavelengths tends to favor luminous SFGs at  $z \gtrsim 2 - 4$  due to the efficient lens selection at bright far-IR fluxes and the negative K-correction at higher redshifts (Negrello et al. 2017). Second, directly studying unlensed galaxies ostensibly requires a significant investment of ALMA time. Hence, the early efforts were made (reasonably) on some of the most luminous SFGs. Examples are the  $\simeq 10 - 100$  milliarcsecond (mas) studies of sub-millimeter galaxies (SMGs) forming stars at  $1300 - 2800 M_\odot \text{yr}^{-1}$  by Iono et al. (2016) and of less luminous SMGs by Hodge et al. (2016); Gullberg et al. (2018); and Hodge et al. (2019). These heroic efforts at the high-resolution frontier start to venture into the regime of typical SFGs at  $z \sim 3$ . Yet, while these SMGs are  $\gtrsim 2 - 5$  times brighter in the far-IR than typical SFGs, interferometric imaging at low-to-moderate signal-to-noise ratios often result in levels of noise that could be mistaken for structure in a smooth disk, hampering the confidence in confirming or ruling out substructures (Hodge et al. 2016; Gullberg et al. 2018). An even larger ALMA time investment is required for the high fidelity imaging needed to confirm (or definitively rule out) the presence of clumps. The challenge is even greater to conduct such a search in typical SFGs at  $z \sim 1 - 3$  that are where most of the stellar mass in the Universe formed.

In this paper, we present unprecedentedly sensitive, 30 mas resolution ALMA 870  $\mu\text{m}$  dust continuum observations of three typical SFGs at  $z \sim 3$ , selected from the Hubble Ultra-Deep Field (HUDF), to study the structure of their obscured star formation at high fidelity. We describe the observations and data reduction in Section 2, present results in Section 3, and put our results in the observational and theoretical context in Section 4. We

adopt a  $\Lambda$ CDM cosmology with  $\Omega_M = 0.3$ ,  $\Omega_\Lambda = 0.7$ , and  $H_0 = 70 \text{ km s}^{-1} \text{ Mpc}^{-1}$ . At  $z = 3$ ,  $1''$  then corresponds to 7.702 kpc. The Chabrier (2003) initial mass function (IMF) is adopted throughout the paper.

## 2. OBSERVATIONS AND DATA REDUCTION

The three galaxies in this sample were selected from the ALMA HUDF Survey at 1.3 mm (Dunlop et al. 2017). This survey provides effectively an unbiased selection by stellar mass ( $M_*$ ) at intermediate redshift, as is evident from the finding by Dunlop et al. (2017) that they detect seven out of nine galaxies in the HUDF that have  $M_* \geq 2 \times 10^{10} M_\odot$  at  $z > 2$ . The native, untapered sensitivity of the survey,  $29 \mu\text{Jy beam}^{-1}$  rms, reaches down to the SFR level of the main sequence; all but one of the 16 galaxies detected in the survey lie within the scatter of the main sequence at their corresponding redshifts (Dunlop et al. 2017; Elbaz et al. 2018). Although the number of sources is modest, the sample is representative of typical SFGs at  $z \sim 2$  undergoing rapid assembly. In the northeast corner of the field lies a fortuitous constellation of three galaxies — UDF1, UDF2, and UDF7 in the Dunlop et al. (2017) nomenclature — that can fit within the  $17''$  primary beam of ALMA at 345 GHz. This affords high-fidelity imaging of three typical SFGs in one 5-hr single-pointing ALMA observation, which we will describe in this section.

### 2.1. ALMA Observations

The ALMA observations were taken in four observing blocks during 2017 November 23 – 24 as part of a Cycle 5 program #2017.1.00001.S. We used the ALMA Band 7 receivers in the single-continuum mode, tuned to a central frequency of 343.5 GHz. Individual spectral windows (SPWs) were centered between 336.5 and 350.5 GHz; each SPW comprises 128 channels and covers 1875 MHz, resulting in 7.5 GHz of aggregate bandwidth. The single pointing is centered on UDF2: RA =  $3^{\text{h}}32^{\text{m}}43.53^{\text{s}}$ , Dec =  $-27^\circ 46' 39''.28$  (ICRS). At this frequency, the primary beam is  $17''.4$  in diameter. This affords good sensitivity at the positions of UDF1 and UDF7, which are  $7''.4$  and  $8''.2$  from the phase center, at which radii the primary beam attenuation correction factors are 0.61 and 0.54, respectively. The observations were carried out using 43 antennas in an extended configuration with baselines ranging from 92 to 8548 m with the 5<sup>th</sup> and 80<sup>th</sup> percentile baseline lengths of  $L_5 = 296$  m and  $L_{80} = 3366$  m, respectively. Following the ALMA Technical Handbook, the maximum recoverable scale,  $\theta_{\text{MRS}} \approx 0.983\lambda/L_5$  (radians), is  $0''.60$  for the array. This is considerably larger than the extent of the dust emission of the targets at 1.3 mm,  $0''.1 - 0''.5$ , based on earlier ALMA observations (Rujopakarn et al. 2016, 2018). Likewise, the nominal resolution of the array,  $\theta_{\text{res}} \approx 0.574\lambda/L_{80}$  (radians), is 31 mas, corresponding to 240 pc at  $z = 3$ .

Each of the four observing blocks was 78 min in duration, with 48 min being on-source. The calibrators were: J0522–3627 for bandpass and flux density scale calibrations; J0348–2749 for phase; and J0329–2357 and J0522–3627 for pointing. The precipitable water vapor was 0.4 – 0.6 mm during the observations. In total, the observations took 5.2 hr, with 3.2 hr being on-source integration.

### 2.2. ALMA Data Calibration and Imaging

We processed the raw visibilities using the ALMA calibration pipeline in CASA (version 5.1.1-5) and imaged the calibrated visibilities with the CASA task `tclean`. We found deconvolution (i.e., application of the CLEAN algorithm) to be necessary to mitigate the sidelobes from the sources because they are detected at peak signal-to-noise ratios as high as  $40 - 50\sigma$ . We experimented extensively with the parameters in `tclean`. The resulting images are insensitive to whether source masking is employed during deconvolution. No artifacts are observed in sources near the primary beam edge. Considering their large separations from the phase center, we further experimented with the `wproject` gridded to take into account the non-coplanar baseline effect (the  $w$  term), but found no significant improvement between the gridded choice of standard versus `wproject` with `wprojplanes` of up to 1024. The flux distribution of UDF1, near the edge of the primary beam, is virtually identical and the peak flux only differs by 1% between the images produced with standard gridded and one with 1024 `wprojplanes`. Additionally, the `tclean` task converged consistently independent of the choices of `niter` or `threshold`. Overall, the resulting images produced from pipeline-calibrated data are of excellent quality, with no image artifacts that would indicate data or calibration issues.

However, a closer inspection reveals that the small-scale structures within individual galaxies do depend on two areas of the imaging parameters. Firstly, the choice of weighting scheme assigned to the visibility points controls the synthesized beam shape and sensitivity of the image. In CASA, the imaging weight is implemented as the `robust` parameter of the `tclean` task, ranging from  $-2$  (uniform weight, smaller beam, lower sensitivity) to  $+2$  (natural weight, larger beam, higher sensitivity), with 0.0 to 0.5 being the commonly adopted value range. Natural weighting (or larger `robust` setting) produces a larger synthesized beam, i.e., spatially broader distribution of flux for a given fiducial sky intensity distribution. In our case, the natural-weight, untapered beam is  $58 \times 46$  mas, whereas `robust = 0.5` produces a beam that is  $42 \times 30$  mas. This difference affects image-based measurement of morphological properties, such as the decomposition of the bulge and disk components using 2D functional fitting as is commonly employed in optical studies, especially when the component of interest has a similar intrinsic size to the beam.

Another, perhaps more subtle, imaging procedure that affects source structure is the multiscale deconvolution (Cornwell 2008; Rau & Cornwell 2011), which is necessary to deconvolve extended sources such as our targets. Multiscale deconvolution, by design, attributes flux to successive, yet discreet scales. Inevitably, the algorithm preferentially attributes flux to the adopted scales (and the `smallscalebias` parameter). In the example of UDF2, we find that the multiscale-cleaned image employing a set of deconvolution scales of 0 (point source), 5, and 15 pixels has 10% lower peak flux and excess flux at the 15-pixel scale, effectively broadening the central component of the source. In this particular situation, the residual image does not necessarily reflect the goodness of fit, because deep cleaning (i.e., very large `niter`) can arbitrarily move residual flux into cleaned components.

This affects the image-based structural parameter measurements (e.g., effective radius and Sérsic index). Because the fiducial structure of the target is not known *a priori* to allow an informed choice of deconvolution scales, and because both single-scale and multi-scale images are faithful representations of the inverse Fourier transform of the interferometric visibilities (as are an infinite number of other images), this poses a dilemma as to which image is a better representation of the true morphology.

We reiterate that the CASA-produced images contain no imaging artifacts and exhibit a clean background noise image, characteristics of high-quality data and calibration. The final CASA image was made with a cell size of 6 mas (i.e., covering the 30 mas synthesized beam with five resolution elements to aid deconvolution), Briggs weighting with the `robust` parameter of 0.5, MFS spectral definition mode, and the Högbom minor cycle algorithm. The primary beam attenuation correction is done with `tclean` during this step. The final image has a synthesized beam of  $42 \times 30$  mas, corresponding to  $320 \times 230$  pc at  $z = 3$  with a position angle of  $77.8^\circ$ . The noise in source-free regions near the phase center of the image is well fit by a Gaussian with a rms of  $11 \mu\text{Jy beam}^{-1}$ .

### 2.3. ALMA visibility-based Data Analysis

Even if we contend with the mild dependence of source structure on the choice of imaging and deconvolution methodology, an inherent limitation of the image-plane analysis is that information from baselines longer than those corresponding to the native synthesized beam (i.e., the median synthesized beam from the entire array) is not fully utilized. Therefore, we opt to carry out quantitative structural analysis in the  $uv$  plane.

We carried out the  $uv$ -based morphological analysis using GILDAS (version `jul18a`, with a modification to fit an arbitrary number of model components). The calibrated visibilities (Section 2.2) were spectrally and temporally averaged, then exported from CASA and imported to GILDAS using the `exportuvfits` and `fits_to_uvt` tasks, respectively. The four spectral windows were then combined using the `uv_average` and `uv_merge` tasks. We fitted source models to the visibilities using the task `uv_fit`, fitting all components of all three galaxies simultaneously, and subtracted the models from the data. Combinations of models in a successive progression of complexity were considered, going from a point source, to circular Gaussian, to elliptical Gaussian, until the residual image no longer contained significant peaks or negative regions  $\gtrsim 3 \sigma$ . All model parameters were free (i.e., no parameter fixing). For example, free parameters of elliptical Gaussian models were the centroid, flux, major/minor axes, and position angle. We note that while this analysis is not susceptible to imaging parameters and has the potential to utilize information from the longest baselines, the lack of *a priori* knowledge of the source model remains. That the final residual image contains no perceivable subtraction artifacts and has rms noise of  $10 \mu\text{Jy beam}^{-1}$ , consistent with that of the source-free region near the phase center of the `tclean` image from CASA, suggests that the models provide a good fit to the sources. Lastly, as CASA produces a more accurate primary beam attenuation model, we use the primary beam information from `tclean` to correct the flux estimates from the  $uv$  fit.

### 2.4. ALMA Astrometric Accuracy and Source Morphology Fidelity

To study source morphologies at tens of mas and compare them to multiwavelength images, it is vital to establish that ALMA’s astrometry is accurate and that the morphology of the source is robust against interferometric artifacts. The astrometric accuracy depends primarily on (1) the signal-to-noise ratio (S/N) of the source in addition to (2) the quality of phase referencing and the positional uncertainty of the phase calibrator. According to the ALMA Technical Handbook, the theoretical astrometric accuracy at a given observing frequency, baseline length, and S/N, is  $\Delta p = 60 \text{ mas} \times (100 \text{ GHz}/\nu_{obs}) \times (10 \text{ km}/B_{max})/\text{S/N}$ , which, for  $\nu_{obs}$  of 343 GHz,  $B_{max}$  of 8.5 km, and  $\text{S/N} \geq 20$ , typical for our observations, is about 1.0 mas. This is already below the accuracy floor achievable with the standard calibration routine, which is 1.4 mas for 350 GHz observations with a baseline of 7.5 km (ALMA Technical Handbook, and the references therein). Because the phase calibrator, J0348–2749, is tied to the International Celestial Reference Frame to within 0.1 mas (ALMA Calibrator Source Catalogue), the standard calibration noise floor dominates the absolute astrometric uncertainties. To confirm the quality of phase referencing and calibrations independently, we measured the positional offset of the ‘check source’ that is observed as a part of each schedule block, J0336–2644, by fitting a circular Gaussian source model to the visibilities using the procedure described in Section 2.3. We found offsets from the phase center in RA and Dec of  $1.07 \pm 0.05$  and  $1.65 \pm 0.04$  mas, respectively, suggesting that the absolute astrometric accuracy is indeed approaching the 1.4-mas floor. This corresponds to 5% of the synthesized beam size or about 11 pc at  $z = 3$ .

Systematic uncertainties of interferometric calibrations (e.g., baseline calibration) can introduce fictitious morphology in a source. We, therefore, need to establish the source morphology fidelity, which, to first order, can be done by confirming that a point source remains point-like through the entire observing setup and calibration. To this end, we inspected the morphology of the phase calibrator, J0348–2749, which has previously been constrained to be point-like at  $uv_{max}$  of at least 1137 k $\lambda$  (ALMA Calibrator Source Catalogue). Our longest baselines are  $\approx 9779$  k $\lambda$ . Confirming the point-like nature of the phase calibrator hence indicates the angular scale above which morphological measurement is robust. Again, a  $uv$ -plane model fitting (Section 2.3) shows that the phase calibrator, detected at  $\simeq 10^4 \sigma$ , is well described by a circular Gaussian with FWHM of  $2.30 \pm 0.02$  mas, i.e., there is no measurable artificial broadening beyond the 2.3 mas scale. We also conducted this experiment on the flux calibrator, J0522–3627, which is detected at  $\simeq 10^5 \sigma$  and found the size to be  $\lesssim 0.5$  mas, although there is a jet-like extended component at the 0.1% flux level. Therefore, we adopt the result from the phase calibrator that the morphology is robust at angular resolutions  $\geq 2.3$  mas. These experiments quantified the fidelities of astrometric and morphological measurements to an angular scale that is a small fraction of the synthesized beam, i.e., to physical scales of  $10 \times 20$  pc at  $z = 3$ . The position and morphology resolved by the beam of  $320 \times 230$  pc can therefore be studied confidently.

TABLE 1  
TYPICAL STAR-FORMING GALAXIES IN THE HUDF

ID	RA (deg)	Dec (deg)	$z$	$M_*$ ( $\log M_\odot$ )	$L_{\text{IR}}$ ( $\log L_\odot$ )	SFR ( $\log M_\odot$ )	$M_{\text{dust}}$ ( $\log M_\odot$ )	$M_{\text{gas}}$ ( $\log M_\odot$ )	$f_{\text{gas}}$	SFR <sub>limit</sub> ( $M_\odot \text{yr}^{-1}$ )
UDF1	53.18347	-27.77666	2.698	$10.7 \pm 0.1$	$12.59 \pm 0.01$	$444 \pm 5$	$9.03 \pm 0.02$	$11.0 \pm 0.2$	$0.7 \pm 0.1$	1.9
UDF2	53.18137	-27.77758	2.696	$10.9 \pm 0.2$	$12.35 \pm 0.01$	$257 \pm 4$	$8.99 \pm 0.03$	$11.0 \pm 0.2$	$0.5 \pm 0.1$	0.9
UDF7	53.18053	-27.77971	2.59	$10.6 \pm 0.2$	$12.01 \pm 0.01$	$116 \pm 1$	$8.33 \pm 0.08$	$10.3 \pm 0.3$	$0.3 \pm 0.2$	2.8

NOTE. —  $f_{\text{gas}} = M_{\text{gas}}/(M_{\text{gas}} + M_*)$ ;  $z_{\text{spec}}$  is reported with three decimal points, two decimal point value indicates  $z_{\text{phot}}$ . Uncertainties of parameters from far-IR SED fitting, e.g.,  $L_{\text{IR}}$  and SFR are statistical. SFR<sub>limit</sub> on substructures is  $1\sigma$  per 200-pc beam, details in Section 3.2. We assume a main-sequence  $M_{\text{gas}}/M_{\text{dust}}$  of 90 here.

### 2.5. Ancillary Data

The HUDF (Beckwith et al. 2006) has a uniquely sensitive set of multiwavelength imaging and spectroscopy. The following is the list of surveys and catalogs used in this work. The *HST* images at  $0.4 - 1.6 \mu\text{m}$  that reach  $29.8 - 30.3 \text{ mag}$  (5 $\sigma$ , AB) are from the HUDF12 and XDF data releases (Ellis et al. 2013; Koekemoer et al. 2013; Illingworth et al. 2013). We have corrected all *HST* images for the astrometric offsets reported by Rujopakarn et al. (2016), derived by comparing the *HST* and VLA positions ( $\Delta\text{RA} = -80 \pm 110 \text{ mas}$ ,  $\Delta\text{Dec} = 260 \pm 130 \text{ mas}$  bring *HST* astrometry to an agreement with the ICRF), which is now confirmed by comparing *HST* positions with those from Pan-STARRS (M. Franco et al., in preparation). *Spitzer* and *Herschel* catalogs at  $3.6 - 500 \mu\text{m}$  are based on the methodology originally discussed in Elbaz et al. (2011); a new, deblended far-IR photometric catalog described by Elbaz et al. (2018) is used in this work. The field has been a subject of intense ALMA contiguous deep-field observations, including, e.g., at 1.3 mm (Dunlop et al. 2017) and ALMA Spectroscopic Survey in the HUDF (APECS; PI: F. Walter) at Bands 3 (84 - 115 GHz) and 6 (212 - 272 GHz). Ultra-deep VLA observations at 6 GHz reach  $0.32 \mu\text{Jy beam}^{-1} \text{ rms}$  (Rujopakarn et al. 2016), detecting all the confirmed<sup>1</sup> Dunlop et al. (2017) ALMA sources at  $z < 4$ . Spectroscopic redshifts are available for UDF1 and 2; an accurate photometric redshift utilizing all available optical and near-infrared imaging is adopted for UDF7. The *Chandra* 7 Ms X-ray survey (Luo et al. 2017) is used to identify X-ray AGNs.

We estimate the spatially-integrated stellar mass ( $M_*$ ) using HYPERZ (Bolzonella et al. 2000) and the Pérez-González et al. (2008) SED fitting codes, utilizing the most recent revision of the Barro et al. (2011) photometric compilation. All photometry out to  $8.0 \mu\text{m}$  is utilized, adopting the Bruzual & Charlot (2003) stellar population synthesis model (hereafter BC03), experimenting with both the constant and exponentially declining star-formation histories, a Chabrier (2003) IMF, and the Calzetti et al. (2000) extinction law with  $A_V$  up to 5 mag. The stellar mass estimates from the two codes agreed within  $0.1 - 0.2 \text{ dex}$ ; we average them into the adopted values tabulated in Table 1. We further find good agreement between these values and those estimated with EAZY (Brammer et al. 2008) using the Conroy et al. (2009) Flexible Stellar Population Synthesis, indicating well constrained stellar masses for these galaxies. We use GALFIT (Peng et al. 2010) to model

and decompose the *HST*  $H_{160}$  images (Illingworth et al. 2013) to estimate the effective radius,  $r_e$ , and the Sérsic index,  $n$ . We fitted all components simultaneously to achieve a uniform residual noise, then subtracted the dominant Sérsic component from the fit to search for any stellar mass substructures. The procedure is discussed in detail in Appendix A.

We estimate total IR luminosities,  $L_{\text{IR}}$ , and dust masses,  $M_{\text{dust}}$ , following Magdis et al. (2012) by fitting the *Spitzer*, *Herschel* (deblended), and ALMA photometry at  $24 - 1300 \mu\text{m}$  with the Draine & Li (2007) models. The total gas mass,  $M_{\text{gas}}$ , for each galaxy, which incorporates both the molecular and atomic phases, is then inferred from its dust mass and the metallicity-dependent dust-to-gas ratio,  $\text{GDR}(Z)$ , conversion factor presented in Magdis et al. (2012). For our sample, we adopt a solar metallicity that corresponds to  $\text{GDR}(Z_\odot) \approx 90$ . The  $M_{\text{gas}}$  estimates assuming  $\text{GDR}(Z_\odot)$  agree within  $\simeq 0.1 - 0.2 \text{ dex}$  with those inferred based on the recipe presented in Scoville et al. (2017) using the monochromatic flux densities at 1.3 mm from Dunlop et al. (2017) because  $870 \mu\text{m}$  no longer firmly lies in the rest-frame Rayleigh-Jeans regime at  $z \geq 2.5$ . The  $L_{\text{IR}}$  is used to estimate the SFR via the Kennicutt (1998) relation, with a factor of 0.66 adjustment to the Chabrier (2003) IMF. We note that the  $L_{\text{IR}}$  estimates from the Draine & Li (2007) models agree within  $\lesssim 0.1 \text{ dex}$  with those from the Rieke et al. (2009) templates. Physical parameters of HUDF galaxies are tabulated in Table 1; CANDELS ID are from Guo et al. (2013); object-specific notes on the ancillary data are as follows.

UDF1 (CANDELS ID: 15669) has  $z_{\text{spec}} = 2.698$  from the ASPECS Band 3 survey (González-López et al. 2019; Aravena et al. 2019; Decarli et al. 2019; Boogaard et al. 2019). It harbors an X-ray AGN with  $L_{\text{X}, 0.5-7 \text{ keV}} = 6.4 \times 10^{43} \text{ erg s}^{-1}$  (intrinsic, absorption-corrected). Its radio luminosity of  $L_{6 \text{ GHz}} = 3.8 \pm 0.2 \times 10^{23} \text{ W Hz}^{-1}$  is consistent with being of star-forming origin (Rieke et al. 2009). UDF1 is a borderline starburst, although its SFR/SFR<sub>MS</sub> is just below  $\approx 4$  (SFR<sub>MS</sub> being the SFR centered on the main sequence given its stellar mass and redshift) independent of the choice of SFR<sub>MS</sub> parameterization (Whitaker et al. 2012; Speagle et al. 2014; Schreiber et al. 2015).

UDF2 (CANDELS ID: 15639) has  $z_{\text{spec}} = 2.696$ , also from the ASPECS. This galaxy is not detected in the 7 Ms *Chandra* X-ray observations; its radio luminosity of  $L_{6 \text{ GHz}} = 3.1 \pm 0.3 \times 10^{23} \text{ W Hz}^{-1}$  is consistent with being of star-forming origin. UDF2 is  $\lesssim 3\times$  above the main sequence regardless of the choice of main-sequence parameterization.

<sup>1</sup> One of the Dunlop et al. (2017) ALMA sources, UDF14, at  $3.7\sigma$  has no radio detection and has not been confirmed in more sensitive ALMA observations.

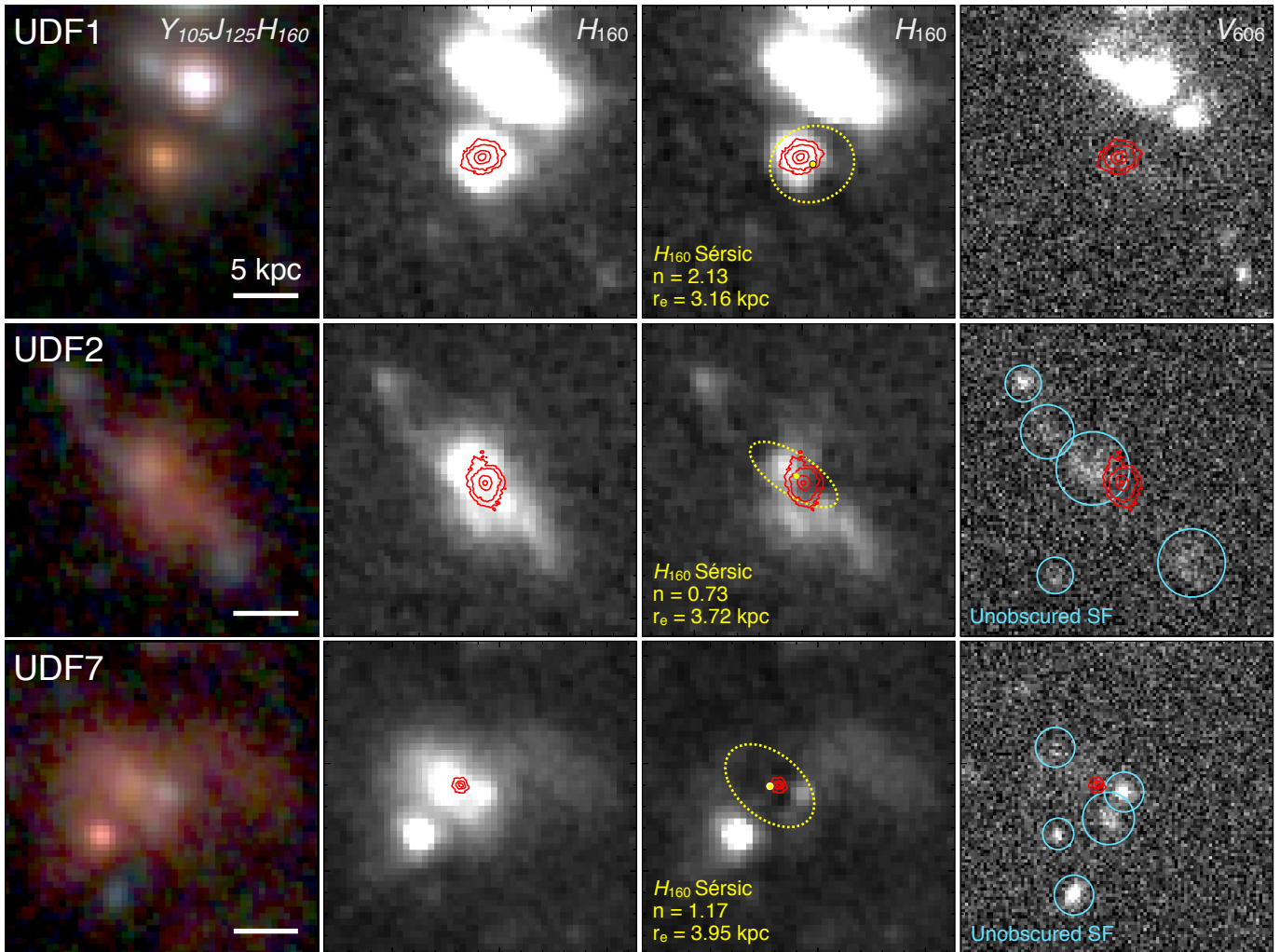


FIG. 1.— The locations of the sites of intense star-formation traced by ALMA (red contours) in relation to the distributions of existing stellar mass and unobscured star formation. From left to right are cutouts from (1) the *HST* color composites with the scale bar indicating a physical scale of 5 kpc; (2) the original *HST*  $H_{160}$  image; (3) the *HST*  $H_{160}$  image with the dominant Sérsic component removed to show stellar mass substructures. The removed Sérsic centroid and size are shown by the yellow dot and yellow ellipse, respectively (details of the GALFIT modeling to quantify this Sérsic in Appendix A); and (4) the *HST*  $V_{606}$  image showing rest-frame UV star formation clumps. Each cutout is  $3'' \times 3''$ ; north is up, east is on the left. The ALMA contours are  $[5, 10, 25, \text{and } 40] \times \sigma$ ; the ALMA beam, not shown, is half the size of the *HST*  $H_{160}$  pixels. The intensely star-forming regions are embedded near the centers of the stellar mass distribution, yet no stellar mass substructures are observed at their locations. The rest-frame UV morphologies of UDF2 and 7 are highly disrupted, with the unobscured star-forming clumps being spatially dislocated by  $\simeq 2 - 10$  kpc from the obscured star-forming disk at the centers.

UDF7 (CANDELS ID: 15381) has  $z_{\text{phot}} = 2.59$ . It is X-ray detected, although its X-ray luminosity of  $L_{X, 0.5-7 \text{ keV}} = 3.7 \times 10^{42} \text{ erg s}^{-1}$  is consistent with being of star-forming origin. The radio luminosity of  $L_{6 \text{ GHz}} = 7.6 \pm 0.2 \times 10^{23} \text{ W Hz}^{-1}$  is  $\sim 5 \times$  the level predicted by the far-IR emission and the far-IR/radio correlation, indicating a radio AGN (Rujopakarn et al. 2018). Its  $\text{SFR}/\text{SFR}_{\text{MS}}$  is  $\lesssim 2 \times$  above the center of the main sequence, again, regardless of the choice of main-sequence parameterization.

### 3. RESULTS

Our ALMA  $870 \mu\text{m}$  observations probe the rest-frame emission at  $\simeq 240 \mu\text{m}$ . No cold dust feature is found at the position of the UV-bright star-forming clumps, which are spatially distanced from the bulk of star formation near the centers (Figure 1). The central regions of intense, obscured star formation in these galaxies are resolved into up to 70 resolution elements (Figure 2).

They are well modeled in the  $uv$  plane with two concentric elliptical Gaussians. We find the distributions of cold dust emission at this physical resolution to be remarkably smooth, showing no sign of clumpy star formation.

#### 3.1. Comparison of ALMA & Optical Morphology

Figure 1 shows ALMA and optical morphologies of the targets. The best-fit model of the cold dust morphology for each galaxy is shown in Figure 2 with parameters tabulated in Table 2; the Sérsic parameters of the dominating component of the  $H_{160}$  morphology are listed in Figure 1. Rest-frame UV clumps are clearly visible in UDF2 and 7 in their *HST*  $V_{606}$  and  $i_{775}$  images. The rest-frame optical features in the *HST*  $Y_{105}$ ,  $J_{125}$ , and  $H_{160}$  images indicate considerable underlying stellar mass. Yet, in all three galaxies, the unobscured star formation traces less than 1% of the total SFR (Dunlop et al. 2017). We note that in comparing the optical and dust distributions, GILDAS measures the ALMA sizes as Gaussian

FWHM,  $\theta$ , whereas GALFIT measures the *HST* sizes as Sérsic effective radius,  $r_e$ . The two conventions are related by  $\theta \sim 2.430r_e$  (Murphy et al. 2017). Morphologies of the individual sources are discussed in detail below.

### 3.1.1. UDF1

Figure 2 shows the rest-frame 240  $\mu\text{m}$  emission of UDF1. The cold dust emission is spatially resolved into  $\simeq 60$  resolution elements (the area enclosed within the FWHM extent). It is best-modeled in the  $uv$  plane by two concentric elliptical Gaussians with integrated fluxes of  $1.56 \pm 0.16$  mJy and  $1.84 \pm 0.16$  mJy (corrected for the primary beam attenuation). Both components are resolved, with FWHMs of  $0.67 \pm 0.04 \times 0.63 \pm 0.03$  kpc and  $1.90 \pm 0.20 \times 1.76 \pm 0.18$  kpc. A single elliptical Gaussian model can only recover 83% of the integrated flux, leaving an extended halo-like residual and necessitating a second, larger component (we will touch on the possibility of the model being a single Sérsic in Section 4.1). After removing these two components, the background noise is uniform; no residual  $\gtrsim 3\sigma$  remains (the local  $\sigma = 15.7 \mu\text{Jy beam}^{-1}$ ).

The *HST*  $H_{160}$  emission is dominated by a point source (i.e., a point-spread function) and a fainter Sérsic component, likely representing the AGN and disk-like emission, respectively. The Sérsic component has an effective radius  $r_e = 3.16 \pm 0.17$  kpc and a Sérsic index  $n = 2.13 \pm 0.13$ . There appears to be an offset of  $0''.13$  between the Sérsic component and the AGN (Figure 1 and Appendix A), which may be a sign of a recent interaction. The cold dust is co-spatial with the AGN/point source. That is, the dust emission is co-spatial with the AGN and offset from the stellar-mass centroid. There are no off-center star-forming clumps in the *HST* rest-frame UV images.

### 3.1.2. UDF2

The rest-frame 240  $\mu\text{m}$  emission of UDF2 is spatially resolved into  $\simeq 70$  resolution elements. The source is well modeled with two concentric elliptical Gaussians: one bright, extended component, and a fainter compact one, nicknamed hereafter as the “disk” and “core”, respectively. The disk is best-modeled by an elliptical Gaussian with a FWHM of  $3.63 \pm 0.17 \times 1.51 \pm 0.09$  kpc, with an integrated flux of  $2.0 \pm 0.1$  mJy. The core is modeled by an elliptical Gaussian with a FWHM of  $0.79 \pm 0.05 \times 0.36 \pm 0.04$  kpc and a flux of  $0.80 \pm 0.05$  mJy. These two components were fitted simultaneously, yielding a combined flux of  $2.80 \pm 0.1$  mJy. After subtracting the core and disk from the image, no residual peak  $\gtrsim 3\sigma$  remains (local  $\sigma = 9.6 \mu\text{Jy beam}^{-1}$ ).

The  $H_{160}$  morphology is significantly disturbed. Full morphological modeling using GALFIT requires fitting simultaneously six components to yield a uniform residual image (model shown in Appendix A). There are two dominant ones: a Sérsic disk and a compact component indicating a substantial concentration of stellar mass. The dominant Sérsic component has an effective radius  $r_e = 3.71 \pm 0.06$  kpc, a Sérsic index  $n = 0.73 \pm 0.04$ , and a position angle of  $56^\circ \pm 1^\circ$ . There is a broad similarity in the orientation of the optical Sérsic component and that of the dust disk,  $\text{PA} = 16^\circ \pm 3^\circ$ . However, the misalignment is significant, undermining the interpretation

that they originate from a common physical structure. Subtracting only the dominant Sérsic component reveals multiple stellar-mass substructures (Figure 1); the dust emission is not co-spatial with any of them. The offset from the dust emission peak to the largest stellar mass concentration is  $\sim 0''.25$ . The offset between the centroid of the best-fit Sérsic component and dust emission is  $\lesssim 1/6^{\text{th}}$  of the effective diameter of the Sérsic component. That is, the cold dust emission appears to originate within the geometric centroid of the stellar distribution that could be characterized as the core area of UDF2. However, the region of dust emission is devoid of stellar-mass substructures, which could be an effect of strong extinction associated with the dust concentration.

None of the remaining four stellar mass substructures coincide with the dust emission; they have a range of offsets of  $0''.3$  to  $1''.3$  ( $2 - 10$  kpc) from its center. These substructures have corresponding counterparts in the *HST*  $i_{775}$  and  $V_{606}$  images that probe the rest-frame emission at  $\simeq 1300 - 2200 \text{ \AA}$ , suggesting that they harbor unobscured star formation. The SFR of these substructures is  $< 1 M_\odot \text{yr}^{-1}$ , less than 0.5% of the total SFR.

### 3.1.3. UDF7

The dust emission of UDF7 is well-modeled with an elliptical Gaussian and a co-spatial point source, with the point source a factor of four fainter than the Gaussian component. The Gaussian FWHM is  $0.90 \pm 0.10 \times 0.29 \pm 0.07$  kpc in size, containing  $0.58 \pm 0.05$  mJy of integrated flux, whereas the point source is  $0.13 \pm 0.03$  mJy (both corrected for the primary beam attenuation). This is an example where the  $uv$ -based analysis is necessary to measure the size of the dust emitting region, as the minor axis of the Gaussian is comparable in size to the native beam. After subtracting the two components, no residual peak  $\gtrsim 3\sigma$  remains (local  $\sigma = 17.6 \mu\text{Jy beam}^{-1}$ ).

The  $H_{160}$  image shows complex morphology, requiring five components to model using GALFIT (Appendix A). The dominant Sérsic component has  $r_e = 3.95 \pm 0.04$  kpc and  $n = 1.17 \pm 0.01$ , with a  $\simeq 0''.1$  offset from the centroid of the dust emission. Nevertheless, given that the dust emission is very compact, it originates entirely from the central area of the stellar mass concentration. There are five distinct rest-UV-bright clumps identifiable in the  $i_{775}$  and  $V_{606}$  images, with counterparts in every band out to  $H_{160}$  indicating considerable underlying stellar mass. No cold dust feature is observed at the positions of these star-forming clumps. The dominant Sérsic component is marginally detected in the  $V_{606}$  image, but it is fainter than the UV star-forming clumps. Again, the unobscured star formation in UDF7 contributes  $< 1 M_\odot \text{yr}^{-1}$  to the global star formation.

## 3.2. Smoothness of the Cold Dust Distributions

Our high-fidelity, extinction-independent observations reveal the central region of intense star formation in each galaxy to be morphologically smooth — in the sense that only the dominant disk-like dust concentration is present with no additional substructure or clumpy appearance. We quantify the upper SFR limit of substructures by scaling the local 870  $\mu\text{m}$  residual noise per beam to the total 870  $\mu\text{m}$  flux, which corresponds to the spatially-integrated SFR estimated from fitting the SED with the

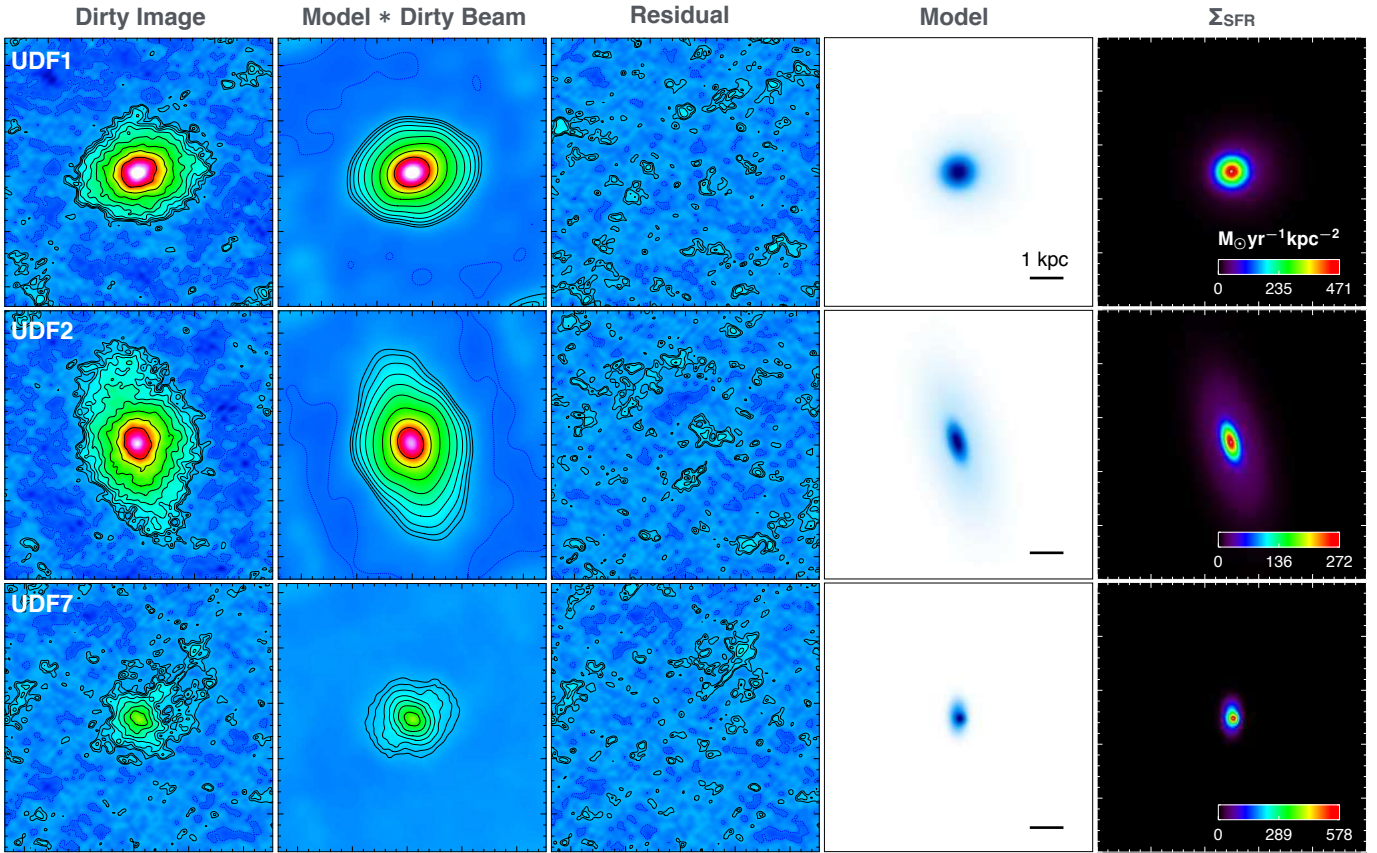


FIG. 2.— The  $uv$ -plane modeling of HUDF galaxies. From left to right: the dirty image; source model convolved with the dirty beam; model-subtracted dirty image; source model; and the  $\Sigma_{\text{SFR}}$  constructed from the model. Each image cutout is  $1'' \times 1''$ ; north is up, east is on the left; the contours are  $[-1.5, 1.5, 1.5^{1.5}, 1.5^2, \dots] \times \sigma$ ; negative contours are dashed. All sources are well-described by the models; the resulting residual noise maps are uniform, indicating the lack of substructures. These images are sensitive to SFRs of  $\simeq 1 - 3 M_{\odot}\text{yr}^{-1}$  per 200-pc beam ( $1\sigma$ ). Substructures at this scale can contain no more than  $\simeq 1 - 8\%$  of the total SFR in these typical SFGs ( $3\sigma$ ).

TABLE 2  
UDF SOURCE DECOMPOSITION IN THE  $uv$  PLANE

ID	Component	RA (")	Dec (")	Flux ( $\mu\text{Jy}$ )	Size (mas)
UDF1	Total	03:32:44.033	-27:46:35.960	$3407 \pm 226$	
	1	$0.003 \pm 0.001$	$0.000 \pm 0.001$	$1844 \pm 159$	$86 \pm 4 \times 82 \pm 4$
	2	$-0.027 \pm 0.009$	$0.005 \pm 0.007$	$1562 \pm 159$	$247 \pm 26 \times 228 \pm 24$
UDF2	Total	03:32:43.529	-27:46:39.275	$2797 \pm 94$	
	1	$0.000 \pm 0.004$	$0.000 \pm 0.007$	$1999 \pm 81$	$457 \pm 21 \times 190 \pm 10$
	2	$0.007 \pm 0.001$	$0.007 \pm 0.002$	$798 \pm 48$	$99 \pm 5 \times 44 \pm 4$
UDF7	Total	03:32:43.326	-27:46:46.963	$704 \pm 56$	
	1	$0.004 \pm 0.004$	$0.001 \pm 0.004$	$576 \pm 48$	$112 \pm 13 \times 36 \pm 9$
	2	$-0.005 \pm 0.003$	$-0.006 \pm 0.002$	$128 \pm 28$	...

NOTE. — Source IDs are from Dunlop et al. (2017). RA and Dec of each component are tabulated as offsets in arcseconds relative to the position (ICRS) in the corresponding ‘Total’ row. Size are FWHM; dots in the size column indicate an unresolved component. Fluxes are  $870 \mu\text{m}$  integrated flux, corrected for the primary beam attenuation.

*Spitzer*, *Herschel*, and ALMA photometry. While this approach assumes that the dust temperature and IMF do not vary within each source, it implicitly takes into account the dust temperature variations among the galaxies. The  $1\sigma$  sensitivities to SFR within our 200-pc beam at the positions of UDF1, 2, and 7 are  $1.9$ ,  $0.9$ ,  $2.8 M_{\odot}\text{yr}^{-1}$ , respectively. That is, the UV-bright clumps can contain no more than  $\simeq 2$ ,  $1$ , and  $8\%$  respectively ( $3\sigma$  upper limits, given the total SFRs in Table 1) of the total star formation in these systems.

Our SFR sensitivity to clumps that are intrinsically larger than the 200-pc beam (e.g.,  $\simeq 1$  kpc) has to be scaled correspondingly (cf. Zanella et al. 2018), as we are limited by the surface brightness sensitivity of our observations. We note that this is a potential issue of the surface brightness limitation and not due to the maximum recoverable scale of the interferometer, which has been shown to be larger than our galaxies in Section 2.1. However, we argue against missing star-forming clumps in this manner with the new findings on the intrinsic clump

sizes via gravitational lensing in Section 4.2.2, comparison with the substructures typically found in SMGs in Section 4.2.3, and with the new model predictions on intrinsic clump sizes in Section 4.2.5.

### 3.3. Maps of Star Formation Rate Surface Density

Maps of the star formation rate surface density,  $\Sigma_{\text{SFR}}$ , are useful for, e.g., combining with  $\Sigma_{M^*}$  measurements to study the spatially-resolved star-formation efficiency, as well as predicting the IR SED of the galaxy (Rujopakarn et al. 2013). We convert the ALMA dust continuum map into one of  $\Sigma_{\text{SFR}}$  by scaling the  $870 \mu\text{m}$  flux to the total in the same way as we placed limits on the clumpy star formation above. Specifically, we constructed a noise-free model for each source from the Gaussian components listed in Table 2.  $\Sigma_{\text{SFR}}$  in each model pixel is given by  $\Sigma_{\text{SFR}} = \text{SFR}_{\text{total}}(S_{870,\text{pixel}}/S_{870,\text{total}})/\Omega_{\text{pixel}}$ , where  $\text{SFR}_{\text{total}}$  is from  $24 - 1300 \mu\text{m}$  SED fitting and  $\Omega_{\text{pixel}}$  is the pixel area in  $\text{kpc}^2$ . As the sources are well described by the Gaussian models, this approach provides a measure of the  $\Sigma_{\text{SFR}}$  that is free of fictitious boosting due to noise fluctuations that could interfere with the interpretation of the maps. The  $\Sigma_{\text{SFR}}$  maps of HUDF galaxies are shown in Figure 2.

These maps indicate that the most intense star formation originates from compact regions: areas with  $\Sigma_{\text{SFR}} \geq 100 M_{\odot}\text{yr}^{-1}\text{kpc}^{-2}$  are limited to the central  $0.4 - 1.0 \text{kpc}^2$  in these galaxies. A majority of the surface area of the dust distribution (i.e., in the sense of an area larger than those enclosed by the FWHM) harbors  $\Sigma_{\text{SFR}} \gtrsim 1 M_{\odot}\text{yr}^{-1}\text{kpc}^{-2}$  and possibly drives strong outflows (e.g., Newman et al. 2012; Bordoloi et al. 2014), to be confirmed with spatially-resolved kinematics.

While this indirect method to produce  $\Sigma_{\text{SFR}}$  maps carries considerable uncertainties, it is the only tracer capable of 200-pc resolution unaffected by dust extinction. If  $A_V$  can indeed be as extreme as  $\sim 100$  mag reported in SMGs (Simpson et al. 2017), this precludes any optical or near-infrared avenues even with the *JWST*: the corresponding  $A_{\text{Pa}\alpha}$  would be  $\sim 15$  mag and  $A_{\text{Br}\alpha}$  would still be  $\sim 2$  mag (Rieke & Lebofsky 1985). An example illustrating the limitations of optical/near-IR tracers is Nelson et al. (2019)’s report of  $\text{H}\alpha$  emission in a  $z \simeq 1.25$  galaxy with a conspicuous void in the middle where, however, the dust continuum indicates intense star formation (see also, e.g., Förster Schreiber et al. 2018). We observe a similar effect in the central region of UDF2, where the  $H_{160}$  emission (rest-frame  $0.43 \mu\text{m}$ ) appears suppressed at the location of dust emission. ALMA remains the only extinction-independent tracer until the era of next-generation radio facilities.

We note that the implicit assumptions that the dust temperature and IMF do not vary spatially within each galaxy are likely to be challenged with future observations. The variation of the dust temperature is straightforward to constrain with additional spatially-resolved observations across the dust spectrum. The IMF variation is less so. Some recent results are hinting a more top-heavy IMF at the sites of intense starbursts locally (Schneider et al. 2018; Motte et al. 2018) and at  $z \sim 2 - 3$  (Zhang et al. 2018). If confirmed to be a common occurrence in typical SFGs at  $z \sim 3$ , this could affect our  $\Sigma_{\text{SFR}}$  estimates.

## 4. DISCUSSION

### 4.1. Spatial distribution of cold dust

While two components were needed to model the cold dust emission of our HUDF galaxies, we did not require them to be co-spatial — their centroids were free parameters. However, the best fit models, yielding uniform noise residual maps, indicate that they are co-spatial within  $\simeq 10$  mas (Table 2), comparable to the corresponding positional uncertainties. It is possible that they can be equally well-modeled by a single Sérsic profile. We will explore this possibility in a future analysis.

On the optical side, we highlight two challenges in interpreting the *HST* morphologies before further discussion of the ALMA/*HST* comparison. First, while disturbed  $H_{160}$  morphologies are observed in all three of our HUDF galaxies (including the visually innocuous UDF1), the origin of such disturbances is inconclusive with the possibilities ranging from in-situ disk instability, patchy dust extinction, to major and minor mergers (or any combinations of these). Second, we cannot ascertain that the rest-frame UV and optical substructures in angular proximity to the galaxies are physically associated with the galaxies (or simply foreground or background sources). Definitive confirmation of associations will require spatially-resolved spectroscopy at resolution comparable to our ALMA observations (tens of mas) from next-generation optical facilities. The following discussion assumes that the rest-frame optical emission modeled with GALFIT (Figure A1 in Appendix A) and the rest-frame UV emission circled in Figure 1 are associated with our galaxies.

For UDF2 and 7, where UV clumps are seen, they are spatially distanced by  $\simeq 2 - 10$  kpc from most of the star formation. The dislocation is a common occurrence in typical  $z \sim 2 - 3$  massive star-forming galaxies (Rujopakarn et al. 2016; Dunlop et al. 2017) and presents a fundamental limitation to the application of an energy-balancing argument (e.g., da Cunha et al. 2015) to estimate their total, mostly obscured, SFR. This effect is also seen in the large dispersion of the infrared excess (IRX) for ALMA-selected galaxies, ranging from the level consistent with the Calzetti et al. (2000) extinction law to 1 – 2 orders of magnitudes above it (McLure et al. 2018), similarly representing an obstacle to the application of the IRX- $\beta$  method ( $\beta$  being the rest-frame UV continuum slope,  $S_{\lambda} \propto \lambda^{\beta}$ ; Meurer et al. 1999) to estimate the total SFR in luminous SFGs typical at this epoch.

In all three galaxies, we observe offsets of  $0'.1 - 0'.2$  between the bulk of star formation and the centroids of the stellar mass distributions. While these offsets are comparable to the  $0'.15$  rms of the registration of *HST* astrometry to the ICRS in GOODS-S, the median offset between *HST* and ICRS is less than 10 mas (Rujopakarn et al. 2016, M. Franco et al., in preparation). Furthermore, the dust location either coincides with the optical AGN (UDF1) or a dark area that may represent strong extinction (UDF2 and 7). These results suggest that the offsets are real, but, e.g., *JWST*/NIRCam imaging will be required for a definitive confirmation. Nevertheless, given the Sérsic sizes and the general proximity of the dust emission to the Sérsic centroids, it can be established with the current imaging that the dust emitting regions are embedded in the Sérsic disk.

While the dust emitting regions are visually more compact than the  $H_{160}$  extent (also reported by, e.g., Chen et al. 2015; Barro et al. 2016; Fujimoto et al. 2018; Hodge et al. 2019), it is possible that the  $H_{160}$  images do not reflect the true stellar mass distribution of these galaxies due to strong dust extinction, especially in the cases of UDF2 and 7. Again, *JWST* and next-generation facilities will be required for a definitive study of the relationship between  $\Sigma_{\text{SFR}}$  and  $\Sigma_{M_*}$ .

Regardless of the fiducial stellar mass distribution at the location of intense star formation, the ongoing episode of star formation is capable of doubling the *global* stellar mass within 0.2 – 0.4 Gyr, and the newly formed stellar mass will likely lie within the innermost  $\lesssim 0.5$  kpc. Whether these episodes of star formation are capable of forming bulges will depend critically on the nature of any feedbacks, e.g., star-formation driven outflows, which remain to be characterized in a spatially-resolved manner in typical SFGs at  $z \sim 3$ .

The intensely star-forming region of UDF7 has previously been reported by Rujopakarn et al. (2018) to be co-spatial with the location of excess radio emission signifying the location of an AGN, which has been localized to  $\lesssim 100$  pc using high-fidelity VLA imaging at 6 GHz (Rujopakarn et al. 2016). We confirm with the improved ALMA imaging in this work that the AGN is co-spatial with intense star-formation at this scale, consistent with a picture of in-situ bulge formation with co-spatial and contemporaneous growth of supermassive black holes. Similarly, the bright point source required to model the  $H_{160}$  morphology of UDF1, which likely represents the AGN emission, is also co-spatial with the dust emission.

Lastly, the smoothness of the cold dust emission is remarkable considering the complex and disturbed the rest-frame UV emission, which indicates that a galaxy-wide disturbance has occurred recently. This highlights how quickly the cold gas is capable of resettling into the star-forming disk following such a disruptive event. While the emergence of a kinematically-ordered disk is anticipated from simulations of, e.g., gas-rich mergers typical in the early Universe after a  $\sim$ Gyr (Robertson et al. 2006; Hopkins et al. 2009) and rotationally-supported disks are observed in local merger remnants (Ueda et al. 2014), the dust disk resettlement timescale of  $\lesssim 0.1$  Gyr implied by the disturbed UV-bright morphology (i.e., the lifetime of OB stars) is not expected from the aforementioned models and suggests that disruptive event in gas-rich environment may be far more dissipative than previously thought. Without drawing a conclusion that our HUDF galaxies are mergers, we nevertheless point out that recent merger simulations such as those of Fensch et al. (2017) that take into account the environment and dynamics typical of the high- $z$  ISM have found the gas resettling time to be  $\sim 0.1 - 0.2$  Gyr. This highlights the importance of characterizing the origin of the disruptive events in these galaxies.

#### 4.2. Clumplessness vs. previously reported clumps

We now put the observed clumplessness of the HUDF galaxies in context by comparing with the previously reported star-forming clumps at various wavelengths, and with the clumps identified from high-resolution images obtained via gravitational lensing. The star formation substructures found in the high-fidelity ALMA observa-

tions of SMGs by Hodge et al. (2019) deserve special attention and will be discussed separately in Section 4.2.3.

##### 4.2.1. Previously reported clumps at various wavelengths

We will first focus on the recent reports of star-forming substructures at  $z \simeq 1 - 3$  from optical and near-IR observations. As clump properties depend strongly on the SFR of their host galaxy, we will discuss the results in the following descending order of SFR: Genzel et al. (2011), Wisnioski et al. (2012), Swinbank et al. (2012), Guo et al. (2018), and Soto et al. (2017).

The Genzel et al. (2011) sample of five typical SFGs is the most similar to our HUDF galaxies in terms of redshift, SFR, and stellar mass:  $z \sim 2.3$ ;  $\text{SFR} \simeq 70 - 180 M_{\odot}\text{yr}^{-1}$ ;  $\log(M_*/M_{\odot}) \simeq 10.3 - 11.0$ . The galaxies are drawn from the spatially-resolved spectroscopic sample of  $\text{H}\alpha$  emission using VLT/SINFONI (Förster Schreiber et al. 2009); additional AO-assisted SINFONI observations were conducted to achieve a typical resolution of  $0''.2$  (Genzel et al. 2011). More than 20 kpc-sized star-forming clumps are found in five galaxies with individual clumps the sites of SFRs of  $3 - 40 M_{\odot}\text{yr}^{-1}$  (typically  $10 - 20 M_{\odot}\text{yr}^{-1}$ ), which are 6 – 20% of the total SFR in each galaxy (we will refer to this percentage as the ‘fractional SFR’ hereafter) based on their  $\text{H}\alpha$  emission. Such star-forming clumps, especially considering their fractional SFR, would have been very strongly detected if any existed in our HUDF galaxies.

Wisnioski et al. (2012) describe a sample at a slightly more recent cosmic epoch,  $z \simeq 1.3$ , and less strong SFRs,  $20 - 50 M_{\odot}\text{yr}^{-1}$ , but similar stellar masses,  $\log(M_*/M_{\odot}) \simeq 10.7 - 11.0$ , i.e., those assembling their stellar mass at relatively later time compared to the Genzel et al. (2011) sample. They find eight clumps in three galaxies from spatially-resolved  $\text{H}\alpha$  observations using Keck/OSIRIS. Overall, their clumps contain a median SFR of  $4 M_{\odot}\text{yr}^{-1}$ , which is 13% in terms of the median fractional SFR. The Swinbank et al. (2012) sample of AO-assisted SINFONI spatially resolved  $\text{H}\alpha$  spectroscopy of nine galaxies drawn from a narrow-band  $\text{H}\alpha$  imaging survey is at a similar redshift of  $z \approx 0.8$  and 1.4 but with a much lower median stellar mass of  $\log(M_*/M_{\odot}) \approx 10.1$ . With the total host SFRs of  $1 - 10 M_{\odot}\text{yr}^{-1}$ , the SFR of individual clumps is also smaller at  $0.5 - 2.9 M_{\odot}\text{yr}^{-1}$ , implying an even larger fractional SFR of  $\sim 25\%$ . Our imaging sensitivity is not sufficient to detect the level of SFRs in the individual Wisnioski et al. (2012) and Swinbank et al. (2012) clumps if they are at  $z = 3$  (possibly detecting 2 – 3 clumps from the former). However, if the fractional SFRs in our targets were as large as in these hosts, they would also have been well detected.

For completeness, we also consider the comprehensive selections of rest-frame UV clumps by Soto et al. (2017) and Guo et al. (2018) using the *HST* rest-frame far-UV and near-UV imaging, respectively. At  $z = 1.5 - 3.0$ , the Guo et al. (2018) catalog contains 1083 clumps in 501 galaxies; the selection bands are the CANDELS imaging at  $V_{606}$  for  $1.0 \leq z \leq 2.0$  and  $i_{775}$  for  $2.0 \leq z \leq 3.0$  galaxies. These clumps have a median  $\log(M_*/M_{\odot})$  of 8.4 (cf. stellar mass of gravitationally lensed star-forming clumps in Section 4.2.2) and a median SFR of the clumps and hosts of  $1.2$  and  $22.2 M_{\odot}\text{yr}^{-1}$ , respectively (7% fractional SFR). At lower redshifts ( $z = 0.5 - 1.5$ ), the Soto et al.

(2017) sample contains typical SFGs selected from the *HST* F225W, F275W, and F336W imaging, with median stellar mass and SFR of  $\simeq 10^7 M_\odot$  and  $0.29 M_\odot \text{yr}^{-1}$ , respectively; again, with a fractional SFR of 5%. We would not be able to detect these unobscured UV clumps if they are at  $z = 3$ , as evident from the optical comparisons in Section 3.1. Two UV clumps in UDF7, the brightest in the optical among our three galaxies, are actually cataloged by Guo et al. (2018), but no dust emission is observed at their locations.

The sensitivity and resolution of sub/millimeter observations have only started to approach optical observations with the advent of ALMA, and still can only reach the more luminous SFR regimes. A majority of high-resolution (e.g., resolution  $\lesssim 0''.2$ ) studies of unlensed galaxies with ALMA were carried out on SMGs selected from single-dish surveys (e.g., the JCMT and APEX surveys of COSMOS, ECDFS, and UDS at  $850 \mu\text{m}$  and  $1.1 \text{ mm}$  by Scott et al. 2008; Weiß et al. 2009; Geach et al. 2017). These surveys pushed their sensitivities to the limit of the confusion noise, typically  $\sim 1 \text{ mJy}$ , yielding reliable detections above sub/millimeter fluxes of  $\sim 4 \text{ mJy}$ , and hence the parent samples for the following observations are populated by luminous SFGs.

Iono et al. (2016) carried out 350 GHz ALMA observations of three sources from the AzTEC survey in COSMOS (AzTEC 1, 4, and 8;  $z = 3.12 - 4.34$ ) with SFR  $\sim 1300 - 2800 M_\odot \text{yr}^{-1}$  at angular resolutions of  $15 - 50 \text{ mas}$ . They reported spatially resolving the sources into multiple substructures; two of the brightest ones in AzTEC-1 (each with SFR  $\simeq 50 M_\odot \text{yr}^{-1}$ ) were confirmed with CO(4-3) kinematics by Tadaki et al. (2018). Hodge et al. (2016) observed 16 sources from the ALESS survey (Hodge et al. 2013) at 354 GHz with  $0''.16$  resolution, revealing them to be extended dust disks with typical diameters of  $3.6 \pm 0.4 \text{ kpc}$ . While a majority of the Hodge et al. (2016) galaxies appear smooth at their resolution and sensitivity, some do show signs of substructures. And even though some of the candidate substructures were later confirmed (Hodge et al. 2019, Section 4.2.3 is dedicated to discussing this result), Hodge et al. (2016) demonstrated with simulations that at moderate S/N of  $5 - 10$ , smooth disks can be broken up into visually-convincing spurious clumps. Similarly, dust continuum and [CII] imaging at  $30 \text{ mas}$  resolution by Gullberg et al. (2018) of four  $z \simeq 4.4 - 4.8$  SMGs, selected from the ECDFS and UDS fields, visually show multitudes of substructures. As with Hodge et al., they caution that there is a significant probability that this result may be consistent with a smooth disk. These studies are reminders that high fidelity observations are required in pushing the resolution and sensitivity of interferometric imaging to search for star-forming substructures.

As a result of the confusion limit, even the comparably faint single-dish-selected SMGs are brighter in the far-IR than typical SFGs: they have typical  $S_{870\mu\text{m}}$  of  $5 - 15 \text{ mJy}$  (Weiß et al. 2009; Hodge et al. 2013), whereas massive main-sequence SFGs have  $S_{870\mu\text{m}}$  of about  $1 - 3 \text{ mJy}$  at  $z \sim 3$  (Scoville et al. 2017, and those in this work). As discussed in the following section, observations of lensed SFGs also provide no solid detections. To date, there is no confirmed report of substructures in the bulk of star formation in typical SFGs at  $z \gtrsim 2$ .

#### 4.2.2. Clumps in gravitationally lensed galaxies

Strong gravitational lensing by a galaxy or galaxy cluster preserves surface brightness while spatially magnifying background sources by a factor of as much as a few hundreds. With proper lens modeling, this technique allows current-generation observing facilities to capture high-resolution details in distant galaxies not otherwise feasible. Highly magnifying lenses are often selected from optical surveys of galaxy clusters by identifying bright, extended arcs (e.g., Gladders & Yee 2005; Bayliss 2012).

Gravitational lensing provides more tests for clumps at lower redshifts ( $z \lesssim 2$ ) and/or at lower SFRs. Recent observations of these lensed ‘giant arcs’ often achieve physical resolution in the source plane of  $\simeq 50 - 100 \text{ pc}$ . For example, Sharon et al. (2012) and Wuyts et al. (2014) observed a giant lensed arc RCSGA0327 with *HST* and Keck/OSIRIS, a  $z = 1.70$  galaxy forming stars at  $29 \pm 8 M_\odot \text{yr}^{-1}$ . Source reconstruction indicated at least seven star-forming clumps, each  $300 - 600 \text{ pc}$  in diameter. In SDSS J1110+6459, a  $z = 2.48$  galaxy with a global SFR of  $8.5 M_\odot \text{yr}^{-1}$ , Johnson et al. (2017a,b) reported 27 clumps, each  $60 - 100 \text{ pc}$  in diameter and forming stars at a few  $10^{-3} M_\odot \text{yr}^{-1}$  (see also, Jones et al. 2010; Menéndez-Delmestre et al. 2013; Livermore et al. 2015; Girard et al. 2018).

Cava et al. (2018) reported 55 star-forming clumps in the ‘Cosmic Snake’, a galaxy at  $z = 1.04$  forming stars at  $30 M_\odot \text{yr}^{-1}$ . The background galaxy is lensed into two images: a highly magnified one with magnifications of tens to more than 200 along the namesake arc, and a much less magnified counter-image that has a magnification of 4.5. The physical resolution that can be reconstructed from the Snake is as small as  $30 \text{ pc}$ , whereas the resolution from the counterimage is limited to  $300 \text{ pc}$  (comparable to *HST*’s). Notably, the clumps identified from the 30-pc image have an average mass of  $\log(M_*/M_\odot) = 8.0$ , compared with  $\log(M_*/M_\odot) = 8.7$  from the 300-pc reconstruction; the sizes of the clumps identified in the 300-pc image are also twice as large (after correcting for the lensing effect). The differences highlight the fictitious increase in clump size and mass when measured at lower resolution due to clusters of smaller clumps blending together into the appearance of larger clumps, even with other systematics mitigated by observing the same background source via a natural lens.

Similar results have been reported by others. Dessauges-Zavadsky et al. (2017) compared luminosities and stellar masses of star-forming clumps identified from unlensed and lensed galaxies from the literature and found a systematic difference. Clump stellar masses from lensed galaxies have median  $\log(M_*/M_\odot) \simeq 7.0$  while the median of those from field galaxies is  $\log(M_*/M_\odot) \simeq 8.9$ . This is also reflected in their median luminosity,  $M_V$ , with distributions peaking at  $M_V \simeq -19$  and  $\simeq -17$  for the field and lensed galaxies, respectively. Field identification of clumps primarily relies on *HST* imaging with spatial resolution of  $0''.1$ , corresponding to  $\simeq 1 \text{ kpc}$  at  $z \sim 1 - 3$ . Dessauges-Zavadsky et al. (2017) suggest that the limited spatial resolution and the propensity of the intrinsically  $\sim 100 \text{ pc}$  star-forming clumps with  $\log(M_*/M_\odot) \sim 7 - 8$  to cluster may be responsible for the appearance of giant kpc clumps with  $\log(M_*/M_\odot) \simeq 9$ . Similarly, Rigby et al. (2017) smoothed the model

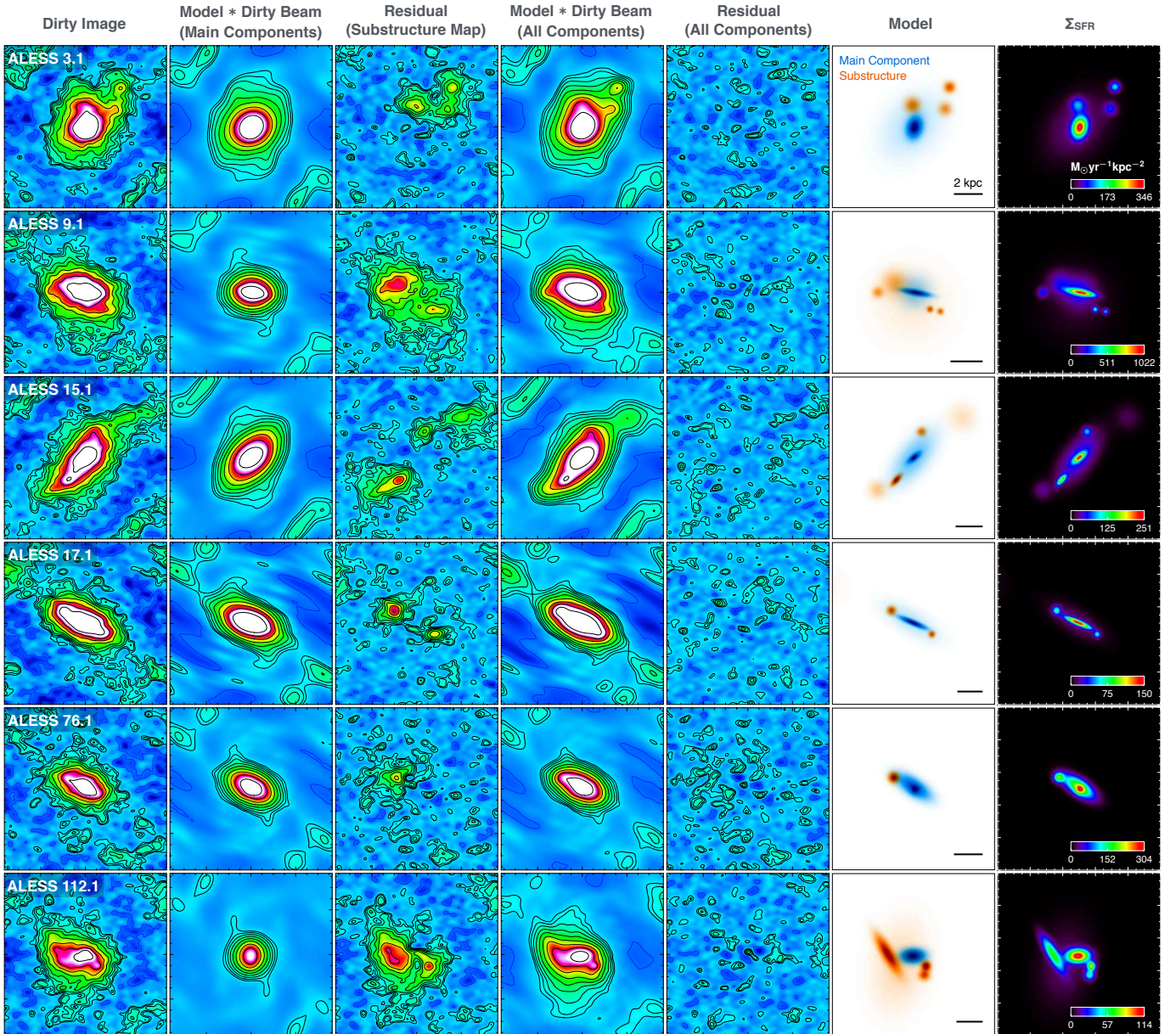


FIG. 3.— Applying the same analysis method as done with the HUDF galaxies (Figure 2), we find that the Hodge et al. (2019) submillimeter-selected galaxies (SMGs) contain not only the dominating disk components, but also multiple substructures (Section 4.2.3). From left to right: dirty image; model convolved with the dirty beam for main components (those marked as “main” components in Table 4); residual after subtracting the main components, i.e., dirty map of substructures; source model convolved with dirty beam for all components; residual after subtracting all components; source model showing the main components in blue and substructures in red;  $\Sigma_{\text{SFR}}$  map. Each image cutout is  $1''.5 \times 1''.5$ ; north is up, east is on the left; the contours are  $[-1.5, 1.5, 1.5^{1.5}, 1.5^2, \dots] \times \sigma$ . Our accurate decomposition of the sources indicates that many of the substructures (red components in the model column) in the Hodge et al. (2019) SMGs are as bright at  $S_{870}$  as our individual HUDF galaxies.

image of SDSS J1110+6459 to simulate the resolution of *HST* and found that the intrinsic 27 clumps were blended together into a single disk with Sérsic index  $n = 1.0 \pm 0.4$  and  $r_e = 2.7 \pm 0.3$  (see also a similar result from smoothing low- $z$  galaxy images to simulate  $z \sim 2$  galaxies by Fisher et al. 2017). It remains an open question whether giant, massive kpc-scale star-forming clumps really do exist and whether clump-clump mergers are capable of producing such massive clumps in their course of evolution. We will revisit the topic of the intrinsic clump sizes from the theoretical perspective in Section 4.2.5.

While the selection of optically-bright giant arcs in

galaxy clusters affords extraordinary magnification to characterize the intrinsic clumps, it also selects hosts with relatively low SFR that are, by necessity, unobscured. The clumps identified are therefore more similar to rest-frame UV clumps such as those described by Soto et al. (2017) and Guo et al. (2018). Again, highly magnified galaxies in the far-IR are needed to probe the substructures in the bulk of star formation in massive main-sequence SFGs such as those of our HUDF targets.

A notable far-IR search for clumps in main-sequence SFGs at  $z > 2$  was conducted on the strongly lensed “Eyelash”. Swinbank et al. (2010) reported four clumps

TABLE 3  
SUBMILLIMETER-SELECTED GALAXIES IN THE HODGE ET AL. (2019) ALESS SAMPLE

ID	RA (deg)	Dec (deg)	$z$	$M_*$ ( $\log M_\odot$ )	$M_{*,\text{H19}}$ ( $\log M_\odot$ )	$L_{\text{IR}}$ ( $\log L_\odot$ )	SFR ( $\log M_\odot$ )	$M_{\text{dust}}$ ( $\log M_\odot$ )	$M_{\text{gas}}$ ( $\log M_\odot$ )	$f_{\text{gas}}$
ALESS 3.1	53.33964	-27.9224	3.374	$10.2 \pm 0.2$	$11.30^{+0.19}_{-0.24}$	$12.89 \pm 0.03$	$880 \pm 30$	$9.45 \pm 0.04$	$10.9 \pm 0.2$	$0.8 \pm 0.1$
ALESS 9.1	53.04722	-27.8700	4.867	$10.8 \pm 0.3$	...	$13.33 \pm 0.06$	$2430 \pm 160$	$9.21 \pm 0.02$	$10.7 \pm 0.2$	$0.4 \pm 0.2$
ALESS 15.1	53.38905	-27.9916	2.67	$10.6 \pm 0.2$	$11.76^{+0.21}_{-0.26}$	$12.62 \pm 0.02$	$470 \pm 10$	$9.65 \pm 0.03$	$11.1 \pm 0.2$	$0.8 \pm 0.1$
ALESS 17.1	53.03035	-27.8558	1.539	$10.8 \pm 0.2$	$11.01^{+0.08}_{-0.07}$	$12.26 \pm 0.05$	$210 \pm 10$	$9.95 \pm 0.03$	$11.4 \pm 0.2$	$0.8 \pm 0.1$
ALESS 76.1	53.38479	-27.9988	3.389	$10.5 \pm 0.3$	$11.08^{+0.29}_{-0.34}$	$12.23 \pm 0.40$	$190 \pm 90$	$9.63 \pm 0.24$	$11.1 \pm 0.4$	$0.8 \pm 0.2$
ALESS 112.1	53.20357	-27.5203	2.315	$11.2 \pm 0.2$	$11.36^{+0.09}_{-0.12}$	$12.57 \pm 0.04$	$420 \pm 20$	$9.57 \pm 0.04$	$11.0 \pm 0.2$	$0.4 \pm 0.1$

NOTE. — Source IDs are from Hodge et al. (2019).  $M_*$  from our estimate using conventional SED fittings and those from H19 based on the energy-balancing MAGPHYS tabulated (except ALESS 9.1 that is affected by blending with a nearby object), details in Section 4.2.4. We assume a starburst  $M_{\text{gas}}/M_{\text{dust}}$  of 30 here.  $f_{\text{gas}} = M_{\text{gas}}/(M_{\text{gas}} + M_*)$ , adopting our  $M_*$  estimates.

of 100 – 300 pc diameter in this gravitationally-lensed typical SFG with a total unlensed SFR of  $210 \pm 50 M_\odot \text{yr}^{-1}$  at  $z = 2.33$ . The reported star-forming substructures are clearly visible at  $4 - 7\sigma$  in their  $870 \mu\text{m}$  image from the Submillimeter Array (SMA; Swinbank et al. 2010). However, recent ALMA observations at multiple bands with higher sensitivity than those from the SMA indicate that the Eyelash is morphologically smooth (Falgarone et al. 2017, Ivison et al., in preparation). While this is a gravitationally lensed system, the disagreement is unrelated to the lens, but rather to the challenges of interferometric imaging.

The most prolific approach to identify far-IR lenses is to conduct large area shallow surveys for far-IR-bright sources. This is because the bright end of the far-IR number counts plummets rapidly above, e.g.,  $S_{500\mu\text{m}}$  of 100 mJy, such that the fraction of lensed galaxies above this range is near unity (Negrello et al. 2017). The largest samples of far-IR lenses were identified from surveys such as the South Pole Telescope (SPT) 87 deg<sup>2</sup> surveys at 1.4 and 2.0 mm (Vieira et al. 2010) and the *Herschel*-ATLAS 570 deg<sup>2</sup> survey at 100 – 500  $\mu\text{m}$  (Eales et al. 2010). Far-IR lenses selected from this approach tend to be luminous SFGs at higher redshifts due to the combination of the aforementioned efficient lens selection at bright far-IR flux and the larger effect of the negative K-correction at  $z \gtrsim 2$ . For example, the Spilker et al. (2016) sample of SPT lenses has a median redshift  $z = 4.3$  and median SFR of  $1100 M_\odot \text{yr}^{-1}$ .

The highest resolution and fidelity observations of a lensed system to date are those of SDP.81 at  $z = 3.0$ , identified from *Herschel*-ATLAS, as a part of the ALMA long baseline campaign (ALMA Partnership et al. 2015), which revealed multiple substructures. Given a Toomre parameter  $Q$  of  $\simeq 0.3$ , SDP.81 is likely a merger system that drives intense SFR of  $\simeq 500 M_\odot \text{yr}^{-1}$  at high star formation efficiency (Swinbank et al. 2015; Dye et al. 2015). Swinbank et al. (2015) and Tamura et al. (2015) reported 5 and 35 star-forming clumps, respectively, from the same data; this apparent disagreement illustrates the challenge in clump identification even with high fidelity data. As with interferometric imaging of star-forming substructures in field galaxies (Section 4.2.1), low S/N clumps in lensed sources are subject to the same pitfalls of a smooth disk being broken into clumps, because gravitational lensing preserves surface brightness. The  $\geq 5\sigma$  clumps reported by Swinbank et al. (2015) are 200 – 300

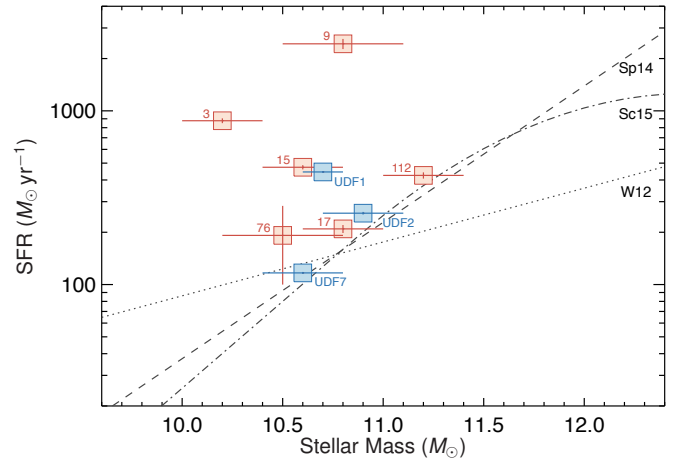


FIG. 4.— Typical star-forming galaxies (SFGs) in the HUDF (blue squares) lie securely within the scatter of the main sequence of SFGs, so do most of the submillimeter-selected galaxies (SMGs) from ALESS in the Hodge et al. (2019) sample (red squares), even considering a very conservative range of possible stellar masses. Both samples also form stars at comparable rates. The main reason that ALESS SMGs are detected in the single-dish survey (which also covers the HUDF) appears to be the larger dust mass. The dotted, dashed, and dot-dashed lines are the main sequence parameterizations at  $z = 3.0$  by Whitaker et al. (2012), Speagle et al. (2014), and Schreiber et al. (2015), labeled W12, Sp14, and Sc15, respectively.

pc in diameter after correcting for lensing effects. Such clumps should be well detected in our ALMA data, given their large fractional SFR (Figure 1 of Swinbank et al. 2015) and the comparable sensitivity between our observations and those of SDP.81 (10 vs. 11  $\mu\text{Jy beam}^{-1}$  rms at Band 7, respectively) to the rest-frame 240 – 250  $\mu\text{m}$  dust continuum. However, SDP.81 is  $\simeq 5$  mJy at 880  $\mu\text{m}$  after correcting for the lensing magnification (Dye et al. 2015, continuum magnification assumed), i.e., more similar in the far-IR flux to SMGs (Section 4.2.3) and 2 – 3 times brighter than our HUDF galaxies. While challenging, future high-fidelity observations similar to those of SDP.81, but on lensed sources identified to be representative of main-sequence SFGs, are needed to study intrinsic clumps in the typical SFG population.

#### 4.2.3. Clumplessness in typical SFGs vs. clumps in SMGs

Hodge et al. (2019), hereafter H19, found multiple clump-like star-forming substructures in six SMGs based on high-fidelity ALMA observations (we use the terms ‘clump’ and ‘substructure’ interchangeably in the follow-

ing discussion). Observationally, the difference between their and our samples is primarily the far-IR flux densities due to the selection from single-dish vs. ALMA deep field observations. As all six H19 SMGs are clumpy, whereas all three SFGs in our sample are clumpless, H19 provides a direct comparison sample to investigate the difference between the two.

The six SMGs are at  $z = 1.53 - 4.86$  in the ECDFS. As with ours, their observations were at  $870 \mu\text{m}$ . They were first identified from a single-dish survey (LESS, Weiß et al. 2009) and followed up with ALMA during Cycle 0 at  $1'' - 3''$  resolution (ALESS, Hodge et al. 2013), from which 16 SMGs were selected for  $0''.16$ -resolution observations by Hodge et al. (2016). From these 16 SMGs, six among the brightest (to minimize the observing time) were selected for 70 mas observations with rms sensitivities of  $22 - 26 \mu\text{Jy beam}^{-1}$ , i.e., same band, approximately a factor of two larger synthesized beam diameter and a factor of two less sensitive than our work.

For a rigorous comparison, we took the pipeline product of the H19 archival data (ALMA#2016.1.00048.S) and analyzed the calibrated visibilities in the  $uv$  plane with GILDAS using the identical procedure as for our data (Section 2.3). We fitted all components of the SMGs simultaneously with all parameters of every component being free. Components were added to the model one-by-one in an increasing order of free parameters (e.g., point, circular Gaussian, elliptical Gaussian); the simultaneous fit was re-run each time as necessary to achieve a uniform residual after subtraction, shown in Figure 3. These components and their parameters are listed in Table 4. The differences between the two data sets are evident: while the HUDF galaxies are well modeled by two cospatial Gaussians, the H19 SMGs require multiple additional small components, confirming the presence of dust substructures reported by H19.

To identify far-IR substructures, we subtract only the dominant components, defined by those positions coinciding with the peak emission. As shown in Table 4, there is little ambiguity as to which components are the dominant ones in all cases except that of ALESS 112.1, where there are two dominant components with integrated fluxes of  $2.0 \pm 0.1$  and  $2.3 \pm 0.2$  mJy; we subtract the former because it is at the location of the peak flux of the source. The substructure maps are shown in Figure 3 along with their source models and the  $\Sigma_{\text{SFR}}$  maps.

Assuming a constant dust temperature and IMF, i.e., that the SFR varies linearly with the rest-frame  $150 - 350 \mu\text{m}$  dust emission, the typical fractional SFRs in substructures range from 4 to 10%, with two substructures being as large as 30–36%. Clearly, this is higher than the 1–8% ( $3\sigma$ ) upper limits in our HUDF galaxies. The average integrated flux of the H19 galaxies from our measurement is 8.0 mJy, whereas the average for HUDF galaxies is 2.3 mJy (cf. Tables 2 and 4). The presence of dust substructures and brighter far-IR fluxes are the two concrete observational differences between the two samples.

The fact that the H19 substructures are found to be as bright (or in some cases brighter) than the entire HUDF galaxies, illustrated in Figure 5, has an important observational implication. Specifically, some of the H19 substructures have comparable  $S_{870\mu\text{m}}$  and physical sizes to our faintest HUDF galaxy, UDF7, e.g., structure# 3 in ALESS 3.1 and structure# 3 in ALESS 17.1, among

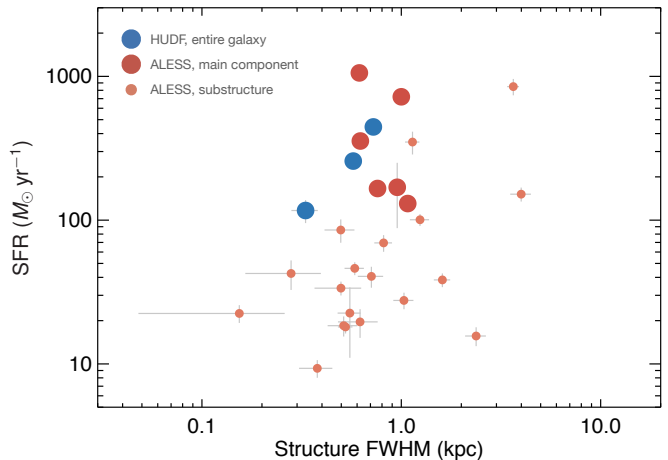


FIG. 5.— As shown in Figures 2 and 3, HUDF galaxies only have smooth components of dust emission, whereas ALESS galaxies have multiple off-center substructures in addition to the main components. Some of the ALESS substructures have comparable sizes and SFRs to an entire HUDF galaxy.

others (Table 4). Since UDF7 is significantly detected ( $\gtrsim 17\sigma$ ), even near the edge of our primary beam, the substructures such as those in the H19 SMGs would also be well detected if they are present in the HUDF galaxies. This negates the concern that the twice higher resolution of our observations (i.e., four times smaller beam area) may lack the surface brightness sensitivity to detect substructures such as those of H19.

#### 4.2.4. How are typical SFGs and SMGs different?

To take a closer look at the physical differences (and commonalities) between our HUDF galaxies and H19 SMGs, we estimate the  $L_{\text{IR}}$ , SFR, and stellar masses of the ALESS sample consistently using the same method as described in Section 2.5 using the most recent photometry and redshift. The most significant revisions in the available data from the previously published estimates are the *HST*  $H_{160}$  photometry from Chen et al. (2015) and the 2-mm photometry from ALMA program# 2015.1.00948.S (PI: da Cunha). The optical-to- $8 \mu\text{m}$  and  $24 - 870 \mu\text{m}$  photometry were taken from Simpson et al. (2014) and Swinbank et al. (2014), respectively, with the addition of the VIDEO and HSC observations (Jarvis et al. 2013; Ni et al. 2019); the  $z_{\text{spec}}$  were from H19.

While the  $M_{\text{dust}}$  and  $L_{\text{IR}}$  are relatively well constrained with the far-IR photometry, estimating the stellar mass is challenging for the H19 SMGs. They are undetected or not significantly detected at any optical/IR bands except at  $3.6 - 8.0 \mu\text{m}$ . As a result, the star-formation history (SFH), age, metallicity, and extinction, on which stellar mass estimates strongly depend, cannot be firmly constrained. In order to quantify the extent of these systematics, we experimented with two independent methods, deriving the ALESS stellar masses using the HYPERZ (Bolzonella et al. 2000) and the Pérez-González et al. (2008) codes (i.e., the same as with the HUDF galaxies in Section 2.5), and compare them with the H19 estimates based on MAGPHYS. For the HYPERZ fit, we adopt a constant SFH, the BC03 models with stellar population age priors ranging from 0.05 – 0.4 Gyr, Chabrier IMF, and the Calzetti attenuation law. For the estimates with the Pérez-González et al. (2008) code, we adopt ex-

TABLE 4  
ALESS SOURCE DECOMPOSITION IN THE  $uv$  PLANE

ID	Component	Type	RA (")	Dec (")	Flux ( $\mu$ Jy)	Size (mas)
ALESS 3.1	Total		03:33:21.514	-27:55:20.466	9134 $\pm$ 308	
	1	Main	0.014 $\pm$ 0.010	0.009 $\pm$ 0.011	4646 $\pm$ 248	541 $\pm$ 29 $\times$ 379 $\pm$ 18
	2	Main	-0.006 $\pm$ 0.001	-0.006 $\pm$ 0.002	2860 $\pm$ 131	150 $\pm$ 5 $\times$ 103 $\pm$ 4
	3	Clump	0.011 $\pm$ 0.005	0.199 $\pm$ 0.005	723 $\pm$ 93	109 $\pm$ 11
	4	Clump	-0.329 $\pm$ 0.005	0.365 $\pm$ 0.004	481 $\pm$ 47	78 $\pm$ 8
ALESS 9.1	5	Clump	-0.289 $\pm$ 0.007	0.164 $\pm$ 0.006	423 $\pm$ 69	95 $\pm$ 13
	Total		03:32:11.332	-27:52:12.005	9767 $\pm$ 590	
	1	Main	-0.022 $\pm$ 0.005	-0.004 $\pm$ 0.001	1535 $\pm$ 139	194 $\pm$ 11 $\times$ 39 $\pm$ 5
	2	Main	-0.009 $\pm$ 0.011	0.003 $\pm$ 0.006	2710 $\pm$ 350	226 $\pm$ 18
	3	Clump	0.177 $\pm$ 0.010	0.085 $\pm$ 0.007	1403 $\pm$ 235	178 $\pm$ 14
	4	Clump	0.017 $\pm$ 0.020	-0.101 $\pm$ 0.025	3409 $\pm$ 381	572 $\pm$ 39
	5	Clump	-0.243 $\pm$ 0.008	-0.177 $\pm$ 0.006	171 $\pm$ 38	44 $\pm$ 17
ALESS 15.1	6	Clump	0.332 $\pm$ 0.007	-0.002 $\pm$ 0.006	343 $\pm$ 59	78 $\pm$ 13
	7	Clump	-0.149 $\pm$ 0.004	-0.158 $\pm$ 0.003	194 $\pm$ 32	...
	Total		03:33:33.371	-27:59:29.720	9471 $\pm$ 252	
	1	Main	0.001 $\pm$ 0.004	0.003 $\pm$ 0.005	6204 $\pm$ 187	440 $\pm$ 5 $\times$ 201 $\pm$ 17
	2	Main	-0.002 $\pm$ 0.003	0.003 $\pm$ 0.002	900 $\pm$ 89	101 $\pm$ 6 $\times$ 40 $\pm$ 8
	3	Clump	0.162 $\pm$ 0.003	-0.205 $\pm$ 0.003	673 $\pm$ 72	95 $\pm$ 9 $\times$ 41 $\pm$ 10
	4	Clump	-0.446 $\pm$ 0.011	0.372 $\pm$ 0.009	768 $\pm$ 81	202 $\pm$ 18
ALESS 17.1	5	Clump	-0.072 $\pm$ 0.005	0.242 $\pm$ 0.004	369 $\pm$ 58	64 $\pm$ 10
	6	Clump	0.337 $\pm$ 0.009	-0.295 $\pm$ 0.007	553 $\pm$ 71	129 $\pm$ 14
	Total		03:32:07.285	-27:51:20.892	9133 $\pm$ 322	
	1	Main	0.024 $\pm$ 0.008	0.015 $\pm$ 0.005	4129 $\pm$ 235	455 $\pm$ 17 $\times$ 174 $\pm$ 9
	2	Main	0.007 $\pm$ 0.002	0.005 $\pm$ 0.001	3121 $\pm$ 178	191 $\pm$ 5 $\times$ 36 $\pm$ 2
	3	Clump	0.206 $\pm$ 0.002	0.118 $\pm$ 0.002	790 $\pm$ 67	62 $\pm$ 5
ALESS 76.1	4	Clump	-0.166 $\pm$ 0.003	-0.102 $\pm$ 0.003	407 $\pm$ 53	44 $\pm$ 8
	5	Clump	0.772 $\pm$ 0.019	0.361 $\pm$ 0.018	683 $\pm$ 96	280 $\pm$ 33
	Total		03:33:32.350	-27:59:55.735	4428 $\pm$ 158	
	1	Main	0.002 $\pm$ 0.004	0.019 $\pm$ 0.003	3594 $\pm$ 117	271 $\pm$ 13 $\times$ 117 $\pm$ 4
	2	Main	-0.008 $\pm$ 0.003	-0.008 $\pm$ 0.002	313 $\pm$ 48	...
ALESS 112.1	3	Clump	0.185 $\pm$ 0.005	0.104 $\pm$ 0.004	521 $\pm$ 93	74 $\pm$ 9
	Total		03:32:48.856	-27:31:13.192	6436 $\pm$ 301	
	1	Main	0.007 $\pm$ 0.003	-0.014 $\pm$ 0.002	1976 $\pm$ 100	170 $\pm$ 8 $\times$ 101 $\pm$ 5
	2	Clump	0.242 $\pm$ 0.005	0.007 $\pm$ 0.007	1524 $\pm$ 131	290 $\pm$ 17 $\times$ 78 $\pm$ 8
	3	Clump	-0.097 $\pm$ 0.007	-0.189 $\pm$ 0.009	297 $\pm$ 66	75 $\pm$ 17
	4	Clump	0.132 $\pm$ 0.020	-0.100 $\pm$ 0.022	2296 $\pm$ 238	627 $\pm$ 63 $\times$ 378 $\pm$ 41
	5	Clump	-0.113 $\pm$ 0.003	-0.108 $\pm$ 0.002	340 $\pm$ 46	18 $\pm$ 12

NOTE. — Source IDs are from Hodge et al. (2019). RA and Dec of each component are tabulated as offsets in arcseconds relative to the phase center position (ICRS) in the corresponding ‘Total’ row. Sizes are FWHM; dots in the size column indicate an unresolved component. Fluxes are integrated, observed-frame 870  $\mu$ m flux.

ponentially declining BC03 models with Chabrier IMF, the Calzetti attenuation law and no assumptions about metallicity. Additionally, we explore a range of  $\tau$  from a single stellar population to constant star formation models;  $A_V$  up to 5 mag is allowed. We find a broad agreement of stellar mass estimates from the two methods, but they are significantly lower (in two cases an order of magnitude lower) than the estimates from MAGPHYS. While some of these differences can be attributed to the assumptions of stellar population properties, both MAGPHYS’ and our approaches could be affected by different pitfalls: ours from not having a firm constraint on dust extinction (whereby  $A_V$  is underestimated), and MAGPHYS from assuming the energy balancing argument despite the dislocations between the stellar mass build-up and intensely star-forming regions (illustrated by the optical/submillimeter comparisons in Figure 2 of H19). As a result, MAGPHYS could systematically overestimate  $A_V$  of any stellar mass build-up that is not co-spatial with the dusty star-forming regions. It is possible that our stellar mass estimates are too low and H19’s too high. The conundrums facing both the conventional and energy-balancing approaches will require *JWST* and next-generation extremely large telescopes to definitively resolve. For the purpose of comparing the H19 and

HUDF samples, we adopt the average of the estimates from our two methods as H19 stellar masses, tabulated in Table 3, along with H19 values for comparison<sup>2</sup>. At the broadest level, this exercise cautions that care is needed in interpreting results pertaining to stellar masses for these extremely dust-obscured SMGs.

Even with a rudimentary constraint on stellar masses, it emerges that four in six H19 SMGs have comparable stellar masses to our HUDF galaxies. These four SMGs are within the scatter of the main sequence (Figure 4), rendering them “typical SFGs” by our definition. They also have similar  $L_{\text{IR}}$ , which could imply similar SFRs barring the probability of top-heavy IMFs at higher  $\Sigma_{\text{SFR}}$  (discussed in Section 3.3). The H19 SMGs appear to have larger dust masses, as evident in the 3 – 5 $\times$  brighter far-IR fluxes (Figure 6). However, this might not be representative of typical submillimeter-selected galaxies because H19 galaxies are among the brightest at the far-IR from the Hodge et al. (2016) sample, which in-turn are among the brightest from the Hodge et al. (2013) sample. Also, their larger dust masses do not necessarily imply larger gas mass, because a lower GDR might be more

<sup>2</sup> For ALESS9.1, the IRAC photometry is blended with a nearby bright object, e.g., Figure 10 of Chen et al. (2015). We estimated the stellar mass with deblended photometry out to 4.5  $\mu$ m

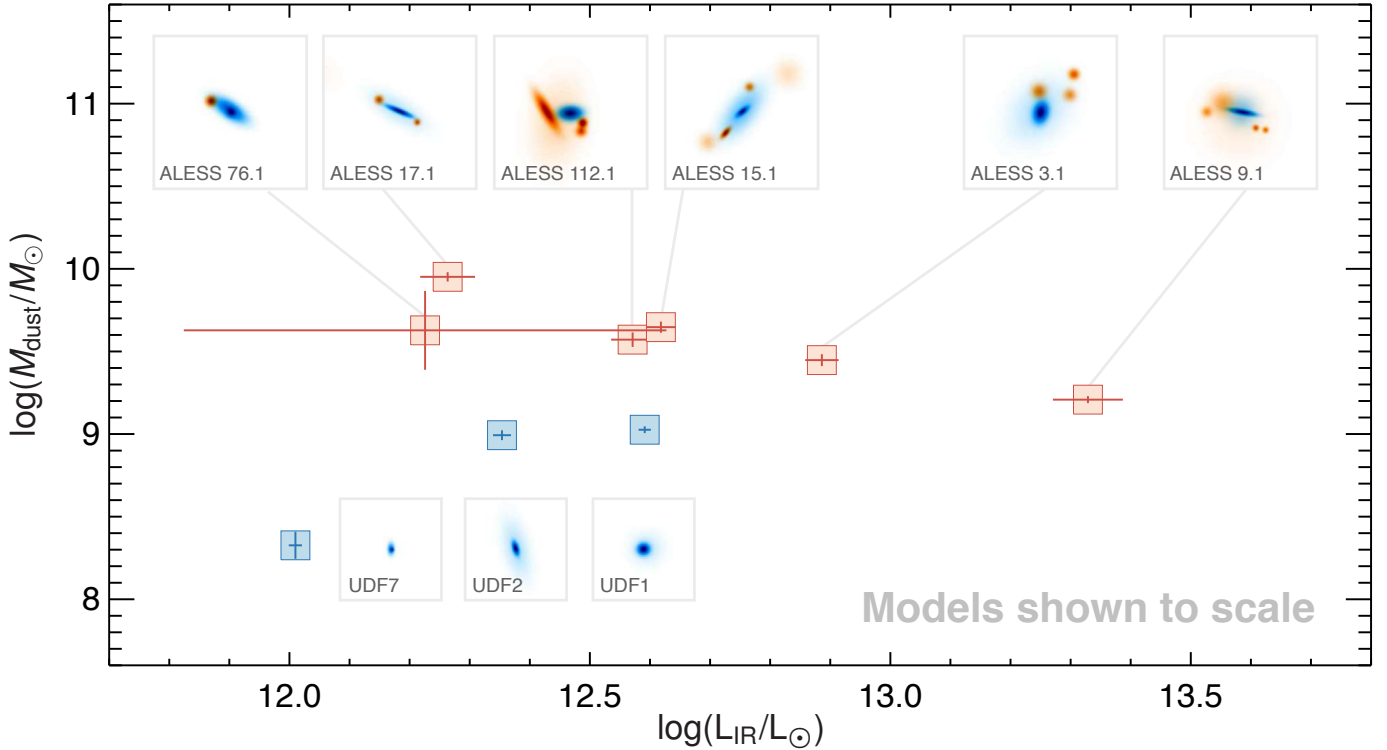


FIG. 6.— Our HUDF galaxies are all clumpless and H19 ALESS SMGs are clumpy with some substructures as large and/or as bright as our HUDF galaxies. A natural explanation is that H19 SMGs are interacting systems involving multiple objects similar to our HUDF galaxies. Furthermore, the significantly larger dust masses of the H19 SMGs could suggest exceptionally intense and/or recent starbursts (Section 4.2.4). Models are shown to the same angular scale; same color coding as in Figures 2 and 3.

appropriate if they are merger-driven starbursts. This is because strong star-bursting systems typically have a CO-to- $M_{\text{gas}}$   $\alpha_{\text{CO}}$  conversion factor of  $0.8 M_{\odot}/(\text{K km s}^{-1} \text{pc}^2)$ , which corresponds to  $\text{GDR} \approx 30$  (e.g., Leroy et al. 2011; Magdis et al. 2012; Genzel et al. 2012; Silverman et al. 2018). It is, therefore, possible that both the ALESS and HUDF samples have comparable gas masses.

Given the comparable  $L_{\text{IR}}$ ,  $M_*$ , and perhaps even  $M_{\text{gas}}$ , between the four out of six H19 SMGs and our HUDF galaxies, why are H19 SMGs much more dust-rich and clumpy? In other words, four of H19 SMGs and our HUDF galaxies are physically similar, so why do they appear differently? An explanation for the H19 substructures being comparably bright to our HUDF galaxies might be that these substructures originated from a class of disruptive event involving multiple systems with dust/gas reservoirs at the scale of our HUDF galaxies, e.g., major mergers of typical SFGs. The scale of the disruptive event found in our HUDF galaxies, characterized by the lack of star-forming substructures at our resolution and sensitivity, could be less violent, e.g., gas-rich disk instability or minor mergers. Rest-frame optical images could provide more insight to the degree of disturbance of the galaxies and whether they are possible merger products. The *HST*  $H_{160}$  imaging of the HUDF galaxies reaches a sensitivity of 29.8 mag AB (Illingworth et al. 2013), but that of the ALESS galaxies has a median sensitivity of only 27.8 mag AB (Chen et al. 2015). More sensitive near-IR images are needed to systematically characterize the morphologies of H19 SMGs.

The picture of H19 SMGs representing a more extreme class of disruptive event that induce exceptionally intense starbursts (even though not all of them are

presently starbursting) might also explain their larger dust mass. A merger-driven starburst in a gas-rich environment could proceed so rapidly compared to its gas re-accretion timescale (e.g., 0.05–0.1 Gyr). As such, dust and metal contents build up quickly in the observed star-forming regions with rapid consumption of gas, leading to a lower GDR even before an appreciable stellar mass increase occurs (see, e.g., the enhanced  $M_{\text{dust}}/M_*$  in starburst galaxies reported by Béthermin et al. 2015). We stress that the proposed scenario is based on a very small number of galaxies. A larger sample of spatially-resolved molecular gas distributions as well as  $\Sigma_{\text{SFR}}$  maps from multiple bands to accurately constrain the  $T_{\text{dust}}$  for a large diversity of SFGs will be vital to testing these possible explanations and are already feasible with ALMA.

#### 4.2.5. Clumplessness vs. models predicting clumps

Our observations of three typical SFGs at  $z \sim 3$ , selected basically on the basis of stellar mass, shows their star formation to be smoothly distributed without significant clumps. This contrasts with the H19 SMGs, selected on the basis of brightness at  $870 \mu\text{m}$ , which finds significant clumpiness in galaxies of similar stellar mass and far-IR luminosity. However, even in these cases, the clumps account for a minority of the far-IR luminosity and hence most of the star formation is not clumpy in both samples. Likewise, the Genzel et al. (2011) images of  $z \simeq 2.3$  galaxies in  $H\alpha$ , whose stellar masses and SFRs are similar to our HUDF SFGs, indicate some clumps (Section 4.2.1) but, again, accounting for only a small fraction of the total SFR. Studies of lensed galaxies (Section 4.2.2) also show no convincing cases where the star formation is largely due to clumps.

When observers started to identify giant clumps at  $z \sim 2$  using *HST* images and found them to be  $\sim 1$  kpc in size and  $\sim 10^9 M_\odot$  in stellar mass, theorists invoked gas fragmentation driven by gravitational instability in gas-rich turbulent disks fed by intense inflows of gas fuel to reproduce such clumps in simulations of both isolated galaxies (Noguchi 1999; Immeli et al. 2004; Bournaud et al. 2007) and in cosmological simulations (Agertz et al. 2009; Ceverino et al. 2010; Genel et al. 2012). As observational evidence is mounting that the apparent giant clumps are likely caused by the limited angular resolution of observing facilities and the modest S/N of the observations, and any clumps are intrinsically an order of magnitude smaller (Section 4.2.2), the spatial and/or temporal resolution of models have also improved by an order of magnitude along with the more realistic sub-grid physics, affording vast improvement in simulation of disk substructures. With the improved models, a new consensus emerged among modelers that typical clumps formed by disk fragmentation should be an order of magnitude smaller than previously thought, with clump mass in the range of  $10^7 - 10^8 M_\odot$  and clump radii of  $100 - 200$  pc (Moody et al. 2014; Mandelker et al. 2014; Mayer et al. 2016; Oklopčić et al. 2017; Mandelker et al. 2017), and that clumps more massive than  $10^9 M_\odot$  are rare, likely the result of clump-clump mergers or further gas accretion (Tamburello et al. 2015, 2017).

To reconcile this prediction of smaller clumps with the observations of kpc-sized clumps, Behrendt et al. (2016) showed that clusters of  $\sim 10$  small clumps, each of  $\sim 10^7 M_\odot$  and  $\sim 70$  pc in diameter, can appear as a single giant clump when observed at the resolution of *HST* and AO-assisted ground-based facilities. Perhaps more importantly, these clump clusters can explain the large velocity dispersions observed in the giant clumps ( $50 - 100$  km s $^{-1}$ , Genzel et al. 2011) as due to the internal motion within the clump cluster, i.e., without having to invoke stellar feedback. Tamburello et al. (2017) constructed mock H $\alpha$  maps from the simulations of Tamburello et al. (2015) and “observed” them at 0.1 and 1 kpc resolutions. They found that the inferred physical properties of clumps depend sensitively on the observing resolution, e.g., the clump masses differ by a factor of two and the typical clump radii by an order of magnitude between the 0.1 and 1 kpc observations.

More recently, Faure et al. (in preparation) have used hydrodynamic simulations with a sub-pc resolution to produce mock observations at “*HST*-like” and “ALMA-like” resolutions, 800 and 200 pc, respectively. At the *HST*-like resolution, the gas disk morphologies are dominated by giant clumps each containing a few percent (up to 5 – 10%) of the galaxy’s gas mass; simulations suggest that these giant gas clumps are the counterparts of optical giant clumps. When observed at the 200-pc resolution of our ALMA observations, these giant clumps break into several smaller clouds. These clouds, resolved in ALMA images, typically contain 0.2 – 0.5% of the total gas mass of their host galaxy, with an upper limit of 1.5%. This picture can be tested with ALMA observations slightly more sensitive than those of our HUDF galaxies on a larger sample. These simulations agree with Dessauges-Zavadsky et al. (2017), Fisher et al. (2017), and Rigby et al. (2017) that the blending of multiple small star-

forming clumps can explain the apparent clumpiness at the kpc-scale. Faure et al. (in preparation) also show that these apparent giant kpc-scale clumps, containing multiple smaller clouds, are not transient chance superpositions but gravitationally bound structures that can be gradually dispersed by stellar feedback and/or migrate toward the galactic bulge.

In addition to ruling out the presence of kpc-scale giant star-forming clumps, our observations are in tension with some of the recent models. Since the intrinsic radii of clumps from simulations and observations of gravitational lens systems are now known to be  $50 - 200$  pc, our 200-pc observations are well-suited for detecting them. For example, the typical in-situ clumps predicted by Mandelker et al. (2017) are  $10^{7.5} - 10^{8.5} M_\odot$  in mass,  $300 - 800$  pc in diameter, and harbor SFR  $\sim 0.1 - 10\%$  of that in the disk. The brighter populations of these predicted clumps should be well detected in our galaxies, contrary to our results. Models predicting lower mass clumps are still consistent with the smooth appearance of our HUDF galaxies. However, the finding that the Eyelash is clumpless (Section 4.2.2) will pose an even stronger tension on clumps, down to a physical scale of  $50 - 100$  pc. That is, while some of these simulations are in agreement with the rest-frame UV clumps revealed by gravitational lenses, the situation remains unconstrained in typical massive main-sequence SFGs at  $z \simeq 3$ .

We note that the clumps in the formative era of the Milky Way that Clarke et al. (2019) propose to explain the present-day  $\alpha$ -abundance bimodality measured by the SDSS/APOGEE survey (Nidever et al. 2014) are  $10^{7.5} - 10^{9.5} M_\odot$  in mass; the predicted distribution peaks at  $10^{8.1} M_\odot$ . The low-mass side of this range is still consistent with our HUDF galaxies being smooth.

## 5. CONCLUSION

We present 200-pc resolution ALMA continuum images at rest-frame  $\simeq 240 \mu\text{m}$  of three typical SFGs at  $z \sim 3$  and compare them with those of six SMGs from observations with comparable image fidelity, whose morphological properties have been derived using a self-consistent procedure. Our results can be summarized as follow.

- Our images trace cold dust, which reveals the central obscured star-forming regions in typical SFGs to have smooth, disk-like morphology  $\simeq 1 - 3$  kpc across. Our images are sensitive to SFR of  $1 - 3 M_\odot \text{yr}^{-1}$  ( $1\sigma$ ) at a 200-pc scale. Any clumps or substructures can contain no more than  $1 - 8\%$  ( $3\sigma$  upper limits) of the total star formation.
- No other peripheral dust substructure is seen outside the intense star-forming region in these three typical SFGs. Two of our HUDF galaxies have in total  $\approx 10$  UV-selected star-forming clumps. These clumps are  $\simeq 2 - 10$  kpc from the intense star-forming region. No enhancement of the dust emission is observed from these UV-selected clumps.
- The absence of dust substructures at the 200-pc scale supports the picture that the apparent kpc-sized star-forming clumps are results of clusters of  $\lesssim 100$  pc sub-clumps blending together due to the  $\simeq 0''.1$  resolution of optical observations. However,

the brighter populations of the model-predicted sub-clumps should already be detectable in our ALMA observations, contrary to our findings.

- In contrast with our HUDF galaxies, SMGs in the Hodge et al. (2019) sample have multiple dust substructures, with individual substructures containing typically 10 – 30% of the total SFR, and being as large as our HUDF galaxies in some cases. A natural explanation is that these SMGs are interacting systems involving multiple objects at the scale of our HUDF SFGs. Nonetheless, clumps account for a minority of the star formation even in these cases.

Additional spatially-resolved ALMA observations of cold gas kinematics will be required to confirm that the disk-like cold gas distributions in typical SFGs are indeed rotationally supported, as well as characterizing the potentially strong outflows, which will be critical to interpreting the roles of these compact, intense central star-forming regions in the formation of the bulge. Our findings that typical SFGs are smooth while SMGs are clumpy are still based on a very small number of galaxies. Significant ALMA time investment will be necessary to construct representative samples of typical SFGs and SMGs with high-fidelity morphological information.

#### ACKNOWLEDGMENTS

The authors would like to thank Jacqueline Hodge, Erica Keller, Fabian Walter, Gergö Popping, and Kamol-

nate Trisupatsilp for helpful discussions. W.R. acknowledges support from the Thailand Research Fund/Office of the Higher Education Commission Grant Number MRG6080294; Chulalongkorn University’s CUniverse and the Ratchadapiseksompot Endowment Fund. P.G.P.-G. acknowledges support from the Spanish Government grant AYA2015-63650-P. G.E.M. acknowledges support from the Villum Fonden research grant 13160 “Gas to stars, stars to dust: tracing star formation across cosmic time”, the Cosmic Dawn Center of Excellence funded by the Danish National Research Foundation and the ERC Consolidator Grant funding scheme (project ConTExt, grant number No. 648179). K.K. and T.W. acknowledge the support from JSPS KAKENHI Grant Number JP17H06130 and the NAOJ ALMA Scientific Research Grant Number 2017-06B. C.C.W. acknowledges support from the NSF Astronomy and Astrophysics Fellowship grant AST-1701546. Kavli IPMU is supported by World Premier International Research Center Initiative (WPI), MEXT, Japan. This paper makes use of the following ALMA data: ADS/JAO.ALMA#2017.1.00001.S, #2016.1.00048.S, #2015.1.00948.S, #2012.1.00173.S. ALMA is a partnership of ESO (representing its member states), NSF (USA) and NINS (Japan), together with NRC (Canada) and NSC and ASIAA (Taiwan) and KASI (Republic of Korea), in cooperation with the Republic of Chile. The Joint ALMA Observatory is operated by ESO, AUI/NRAO and NAOJ.

#### REFERENCES

- ALMA Partnership, Vlahakis, C., Hunter, T. R., et al. 2015, *ApJ*, 808, L4
- Agertz, O., Teyssier, R., & Moore, B. 2009, *MNRAS*, 397, L64
- Aravena, M., Decarli, R., González-López, J., et al. 2019, arXiv:1903.09162
- Barro, G., Pérez-González, P. G., Gallego, J., et al. 2011, *The Astrophysical Journal Supplement Series*, 193, 13.
- Barro, G., Kriek, M., Pérez-González, P. G., et al. 2016, *ApJ*, 827, L32
- Bayliss, M. B. 2012, *ApJ*, 744, 156
- Beckwith, S. V. W., Stievelli, M., Koekemoer, A. M., et al. 2006, *AJ*, 132, 1729
- Behrendt, M., Burkert, A., & Schartmann, M. 2016, *ApJ*, 819, L2
- Behroozi, P. S., Wechsler, R. H., & Conroy, C. 2013, *ApJ*, 770, 57
- Béthermin, M., Daddi, E., Magdis, G., et al. 2015, *A&A*, 573, A113
- Bolzonella, M., Miralles, J.-M., & Pelló, R. 2000, *A&A*, 363, 476
- Boogaard, L. A., Decarli, R., González-López, J., et al. 2019, arXiv:1903.09167
- Bordoloi, R., Lilly, S. J., Hardmeier, E., et al. 2014, *ApJ*, 794, 130
- Bournaud, F., Elmegreen, B. G., & Elmegreen, D. M. 2007, *ApJ*, 670, 237
- Bournaud, F., Daddi, E., Elmegreen, B. G., et al. 2008, *A&A*, 486, 741
- Bournaud, F., Perret, V., Renaud, F., et al. 2014, *ApJ*, 780, 57
- Brammer, G. B., van Dokkum, P. G., & Coppi, P. 2008, *ApJ*, 686, 1503
- Brinchmann, J., Charlot, S., White, S. D. M., et al. 2004, *MNRAS*, 351, 1151
- Bruzual, G., & Charlot, S. 2003, *MNRAS*, 344, 1000
- Calzetti, D., Armus, L., Bohlin, R. C., et al. 2000, *ApJ*, 533, 682
- Cava, A., Schaerer, D., Richard, J., et al. 2018, *Nature Astronomy*, 2, 76
- Ceverino, D., Dekel, A., & Bournaud, F. 2010, *MNRAS*, 404, 2151
- Chabrier, G. 2003, *PASP*, 115, 763
- Chen, C.-C., Smail, I., Swinbank, A. M., et al. 2015, *ApJ*, 799, 194
- Cibinel, A., Daddi, E., Bournaud, F., et al. 2017, *MNRAS*, 469, 4683
- Clarke, A. J., Debattista, V. P., Nidever, D. L., et al. 2019, *MNRAS*,
- Conselice, C. J. 2003, *ApJS*, 147, 1
- Cornwell, T. J. 2008, *IEEE Journal of Selected Topics in Signal Processing*, 2, 793
- Conroy, C., Gunn, J. E., & White, M. 2009, *ApJ*, 699, 486
- Cowie, L. L., Hu, E. M., & Songaila, A. 1995, *AJ*, 110, 1576
- da Cunha, E., Walter, F., Smail, I. R., et al. 2015, *ApJ*, 806, 110
- Decarli, R., Walter, F., González-López, J., et al. 2019, arXiv:1903.09164
- Dekel, A., Birnboim, Y., Engel, G., et al. 2009, *Nature*, 457, 451
- Dessauges-Zavadsky, M., Schaerer, D., Cava, A., Mayer, L., & Tamburello, V. 2017, *ApJ*, 836, L22
- Draine, B. T., & Li, A. 2007, *ApJ*, 657, 810
- Dunlop, J. S., McLure, R. J., Biggs, A. D., et al. 2017, *MNRAS*, 466, 861
- Dye, S., Furlanetto, C., Swinbank, A. M., et al. 2015, *MNRAS*, 452, 2258
- Eales, S., Dunne, L., Clements, D., et al. 2010, *PASP*, 122, 499
- Elbaz, D., Dickinson, M., Hwang, H. S., et al. 2011, *A&A*, 533, A119
- Elbaz, D., Leiton, R., Nagar, N., et al. 2018, *A&A*, 616, A110
- Ellis, R. S., McLure, R. J., Dunlop, J. S., et al. 2013, *ApJ*, 763, L7
- Elmegreen, B. G., & Elmegreen, D. M. 2005, *ApJ*, 627, 632
- Elmegreen, D. M., Elmegreen, B. G., Ravindranath, S., & Coe, D. A. 2007, *ApJ*, 658, 763
- Elmegreen, B. G., Elmegreen, D. M., Fernandez, M. X., & Lomonias, J. J. 2009, *ApJ*, 692, 12
- Elmegreen, D. M., Elmegreen, B. G., Marcus, M. T., et al. 2009, *ApJ*, 701, 306
- Falgarone, E., Zwaan, M. A., Godard, B., et al. 2017, *Nature*, 548, 430
- Fensch, J., Renaud, F., Bournaud, F., et al. 2017, *MNRAS*, 465, 1934

- Fisher, D. B., Glazebrook, K., Damjanov, I., et al. 2017, *MNRAS*, 464, 491
- Förster Schreiber, N. M., Genzel, R., Bouché, N., et al. 2009, *ApJ*, 706, 1364
- Förster Schreiber, N. M., Shapley, A. E., Genzel, R., et al. 2011, *ApJ*, 739, 45
- Förster Schreiber, N. M., Renzini, A., Mancini, C., et al. 2018, *ApJS*, 238, 21
- Fujimoto, S., Ouchi, M., Kohno, K., et al. 2018, *ApJ*, 861, 7.
- Gabor, J. M., & Bournaud, F. 2013, *MNRAS*, 434, 606
- Geach, J. E., Dunlop, J. S., Halpern, M., et al. 2017, *MNRAS*, 465, 1789
- Genel, S., Naab, T., Genzel, R., et al. 2012, *ApJ*, 745, 11
- Genzel, R., Burkert, A., Bouché, N., et al. 2008, *ApJ*, 687, 59
- Genzel, R., Newman, S., Jones, T., et al. 2011, *ApJ*, 733, 101
- Genzel, R., Tacconi, L. J., Combes, F., et al. 2012, *ApJ*, 746, 69
- Girard, M., Dessauges-Zavadsky, M., Schaerer, D., et al. 2018, *A&A*, 619, A15
- Gladders, M. D., & Yee, H. K. C. 2005, *ApJS*, 157, 1
- González-López, J., Decarli, R., Pavesi, R., et al. 2019, arXiv:1903.09161
- Grazian, A., Fontana, A., Santini, P., et al. 2015, *A&A*, 575, A96
- Gullberg, B., Swinbank, A. M., Smail, I., et al. 2018, *ApJ*, 859, 12
- Guo, Y., Giavalisco, M., Ferguson, H. C., Cassata, P., & Koekemoer, A. M. 2012, *ApJ*, 757, 120
- Guo, Y., Ferguson, H. C., Giavalisco, M., et al. 2013, *ApJS*, 207, 24
- Guo, Y., Ferguson, H. C., Bell, E. F., et al. 2015, *ApJ*, 800, 39
- Guo, Y., Rafelski, M., Bell, E. F., et al. 2018, *ApJ*, 853, 108
- Heckman, T. M., & Best, P. N. 2014, *ARA&A*, 52, 589
- Hodge, J. A., Karim, A., Smail, I., et al. 2013, *ApJ*, 768, 91
- Hodge, J. A., Swinbank, A. M., Simpson, J. M., et al. 2016, *ApJ*, 833, 103
- Hodge, J. A., Smail, I., Walter, F., et al. 2018, arXiv:1810.12307
- Hopkins, P. F., Cox, T. J., Younger, J. D., & Hernquist, L. 2009, *ApJ*, 691, 1168
- Ikarashi, S., Ivison, R. J., Caputi, K. I., et al. 2015, *ApJ*, 810, 133
- Illingworth, G. D., Magee, D., Oesch, P. A., et al. 2013, *ApJS*, 209, 6
- Immeli, A., Samland, M., Westera, P., & Gerhard, O. 2004, *ApJ*, 611, 20
- Inoue, S., Dekel, A., Mandelker, N., et al. 2016, *MNRAS*, 456, 2052
- Iono, D., Yun, M. S., Aretxaga, I., et al. 2016, *ApJ*, 829, L10
- Jarvis, M. J., Bonfield, D. G., Bruce, V. A., et al. 2013, *MNRAS*, 428, 1281
- Johnson, T. L., Rigby, J. R., Sharon, K., et al. 2017, *ApJ*, 843, L21
- Johnson, T. L., Sharon, K., Gladders, M. D., et al. 2017, *ApJ*, 843, 78
- Jones, T. A., Swinbank, A. M., Ellis, R. S., Richard, J., & Stark, D. P. 2010, *MNRAS*, 404, 1247
- Kennicutt, R. C., Jr. 1998, *ApJ*, 498, 541
- Kereš, D., Katz, N., Weinberg, D. H., & Davé, R. 2005, *MNRAS*, 363, 2
- Koekemoer, A. M., Ellis, R. S., McLure, R. J., et al. 2013, *ApJS*, 209, 3
- Leroy, A. K., Bolatto, A., Gordon, K., et al. 2011, *ApJ*, 737, 12
- Lindroos, L., Knudsen, K. K., Fan, L., et al. 2016, *MNRAS*, 462, 1192
- Livermore, R. C., Jones, T., Richard, J., et al. 2012, *MNRAS*, 427, 688
- Livermore, R. C., Jones, T. A., Richard, J., et al. 2015, *MNRAS*, 450, 1812
- Luo, B., Brandt, W. N., Xue, Y. Q., et al. 2017, *ApJS*, 228, 2
- Madau, P., & Dickinson, M. 2014, *ARA&A*, 52, 415
- Magdis, G. E., Daddi, E., Béthermin, M., et al. 2012, *ApJ*, 760, 6
- Mandelker, N., Dekel, A., Ceverino, D., et al. 2014, *MNRAS*, 443, 3675
- Mandelker, N., Dekel, A., Ceverino, D., et al. 2017, *MNRAS*, 464, 635
- Martig, M., Bournaud, F., Teyssier, R., & Dekel, A. 2009, *ApJ*, 707, 250
- Mayer, L., Tamburello, V., Lupi, A., et al. 2016, *ApJ*, 830, L13
- McLure, R. J., Dunlop, J. S., Cullen, F., et al. 2018, *MNRAS*, 476, 3991
- Menéndez-Delmestre, K., Blain, A. W., Swinbank, M., et al. 2013, *ApJ*, 767, 151
- Meurer, G. R., Heckman, T. M., & Calzetti, D. 1999, *ApJ*, 521, 64
- Momcheva, I. G., Brammer, G. B., van Dokkum, P. G., et al. 2016, *ApJS*, 225, 27
- Moody, C. E., Guo, Y., Mandelker, N., et al. 2014, *MNRAS*, 444, 1389 s
- Motte, F., Nony, T., Louvet, F., et al. 2018, *Nature Astronomy*, 2, 478
- Murphy, E. J., Momjian, E., Condon, J. J., et al. 2017, *ApJ*, 839, 35
- Muxlow, T. W. B., Richards, A. M. S., Garrington, S. T., et al. 2005, *MNRAS*, 358, 1159
- Negrello, M., Amber, S., Amvrosiadis, A., et al. 2017, *MNRAS*, 465, 3558
- Ni, Q., Timlin, J., Brandt, W. N., & Yang, G. 2019, *Research Notes of the American Astronomical Society*, 3, 5
- Nidever, D. L., Bovy, J., Bird, J. C., et al. 2014, *ApJ*, 796, 38
- Nelson, E. J., Tadaki, K.-i., Tacconi, L. J., et al. 2019, *ApJ*, 870, 130
- Newman, S. F., Genzel, R., Förster-Schreiber, N. M., et al. 2012, *ApJ*, 761, 43
- Noeske, K. G., Weiner, B. J., Faber, S. M., et al. 2007, *ApJ*, 660, L43
- Noguchi, M. 1999, *ApJ*, 514, 77
- Oklopčić, A., Hopkins, P. F., Feldmann, R., et al. 2017, *MNRAS*, 465, 952
- Oteo, I., Zwaan, M. A., Ivison, R. J., Smail, I., & Biggs, A. D. 2017, *ApJ*, 837, 182
- Peng, C. Y., Ho, L. C., Impey, C. D., & Rix, H.-W. 2010, *AJ*, 139, 2097
- Pérez-González, P. G., Rieke, G. H., Villar, V., et al. 2008, *ApJ*, 675, 234
- Robertson, B., Bullock, J. S., Cox, T. J., et al. 2006, *ApJ*, 645, 986
- Rodighiero, G., Daddi, E., Baronchelli, I., et al. 2011, *ApJ*, 739, L40
- Rau, U., & Cornwell, T. J. 2011, *A&A*, 532, A71
- Rieke, G. H., & Lebofsky, M. J. 1985, *ApJ*, 288, 618
- Rieke, G. H., Alonso-Herrero, A., Weiner, B. J., et al. 2009, *ApJ*, 692, 556
- Rigby, J. R., Johnson, T. L., Sharon, K., et al. 2017, *ApJ*, 843, 79
- Rujopakarn, W., Rieke, G. H., Eisenstein, D. J., & Juneau, S. 2011, *ApJ*, 726, 93
- Rujopakarn, W., Rieke, G. H., Weiner, B. J., et al. 2013, *ApJ*, 767, 73
- Rujopakarn, W., Dunlop, J. S., Rieke, G. H., et al. 2016, *ApJ*, 833, 12
- Rujopakarn, W., Nyland, K., Rieke, G. H., et al. 2018, *ApJ*, 854, L4
- Salim, S., Rich, R. M., Charlot, S., et al. 2007, *ApJS*, 173, 267
- Salmon, B., Papovich, C., Finkelstein, S. L., et al. 2015, *ApJ*, 799, 183
- Schaye, J., Crain, R. A., Bower, R. G., et al. 2015, *MNRAS*, 446, 521
- Schneider, F. R. N., Sana, H., Evans, C. J., et al. 2018, *Science*, 359, 69
- Schreiber, C., Pannella, M., Elbaz, D., et al. 2015, *A&A*, 575, A74
- Scott, K. S., Austermann, J. E., Perera, T. A., et al. 2008, *MNRAS*, 385, 2225
- Scoville, N., Sheth, K., Aussel, H., et al. 2016, *ApJ*, 820, 83
- Scoville, N., Lee, N., Vanden Bout, P., et al. 2017, *ApJ*, 837, 150
- Silverman, J. D., Daddi, E., Rujopakarn, W., et al. 2018, *ApJ*, 868, 75
- Simpson, J. M., Swinbank, A. M., Smail, I., et al. 2014, *ApJ*, 788, 125
- Simpson, J. M., Smail, I., Swinbank, A. M., et al. 2015, *ApJ*, 799, 81
- Simpson, J. M., Smail, I., Swinbank, A. M., et al. 2017, *ApJ*, 839, 58
- Sharon, K., Gladders, M. D., Rigby, J. R., et al. 2012, *ApJ*, 746, 161
- Soto, E., de Mello, D. F., Rafelski, M., et al. 2017, *ApJ*, 837, 6
- Speagle, J. S., Steinhardt, C. L., Capak, P. L., & Silverman, J. D. 2014, *ApJS*, 214, 15
- Spilker, J. S., Marrone, D. P., Aravena, M., et al. 2016, *ApJ*, 826, 112

Springel, V., Pakmor, R., Pillepich, A., et al. 2018, MNRAS, 475, 676  
 Somerville, R. S., & Davé, R. 2015, ARA&A, 53, 51  
 Stott, J. P., Swinbank, A. M., Johnson, H. L., et al. 2016, MNRAS, 457, 1888  
 Swinbank, A. M., Smail, I., Longmore, S., et al. 2010, Nature, 464, 733  
 Swinbank, A. M., Smail, I., Sobral, D., et al. 2012, ApJ, 760, 130  
 Swinbank, A. M., Simpson, J. M., Smail, I., et al. 2014, MNRAS, 438, 1267  
 Swinbank, A. M., Dye, S., Nightingale, J. W., et al. 2015, ApJ, 806, L17  
 Tadaki, K., Iono, D., Yun, M. S., et al. 2018, Nature, 560, 613  
 Tamura, Y., Oguri, M., Iono, D., et al. 2015, PASJ, 67, 72  
 Tamburello, V., Mayer, L., Shen, S., & Wadsley, J. 2015, MNRAS, 453, 2490  
 Tamburello, V., Rahmati, A., Mayer, L., et al. 2017, MNRAS, 468, 4792  
 van den Bergh, S., Abraham, R. G., Ellis, R. S., et al. 1996, AJ, 112, 359

Ueda, J., Iono, D., Yun, M. S., et al. 2014, ApJS, 214, 1  
 Vieira, J. D., Crawford, T. M., Switzer, E. R., et al. 2010, ApJ, 719, 763  
 Weiß, A., Kovács, A., Coppin, K., et al. 2009, ApJ, 707, 1201  
 Wisnioski, E., Glazebrook, K., Blake, C., et al. 2012, MNRAS, 422, 3339  
 Wisnioski, E., Förster Schreiber, N. M., Wuyts, S., et al. 2015, ApJ, 799, 209  
 Whitaker, K. E., van Dokkum, P. G., Brammer, G., & Franx, M. 2012, ApJ, 754, L29  
 Wuyts, S., Förster Schreiber, N. M., van der Wel, A., et al. 2011, ApJ, 742, 96  
 Wuyts, S., Förster Schreiber, N. M., Genzel, R., et al. 2012, ApJ, 753, 114  
 Wuyts, E., Rigby, J. R., Gladders, M. D., & Sharon, K. 2014, ApJ, 781, 61  
 Zanella, A., Daddi, E., Magdis, G., et al. 2018, MNRAS, 481, 1976  
 Zhang, Z.-Y., Romano, D., Ivison, R. J., et al. 2018, Nature, 558, 260.

## APPENDIX

A. GALFIT MODELING OF *HST*  $H_{160}$  IMAGES

To search for stellar mass substructures, we model the *HST*/WFC3  $H_{160}$  images with GALFIT (Peng et al. 2010) using the procedure illustrated in Figure A1. Starting with the original image in column (a), we model the emission with a combination of multiple Sérsic and/or point sources as necessary to achieve a uniform residual. The best-fit model and the resulting residual are shown in columns (b) and (c), respectively. From these best-fit models, we subtract only the dominant Sérsic components, shown in column (d), to produce the stellar mass substructure maps in column (e). These are the maps shown in the third column from the left of Figure 1, along with the Sérsic index  $n$  and effective radius  $r_e$  overlaid in the corresponding cutout. All images are shown with an identical linear scale.

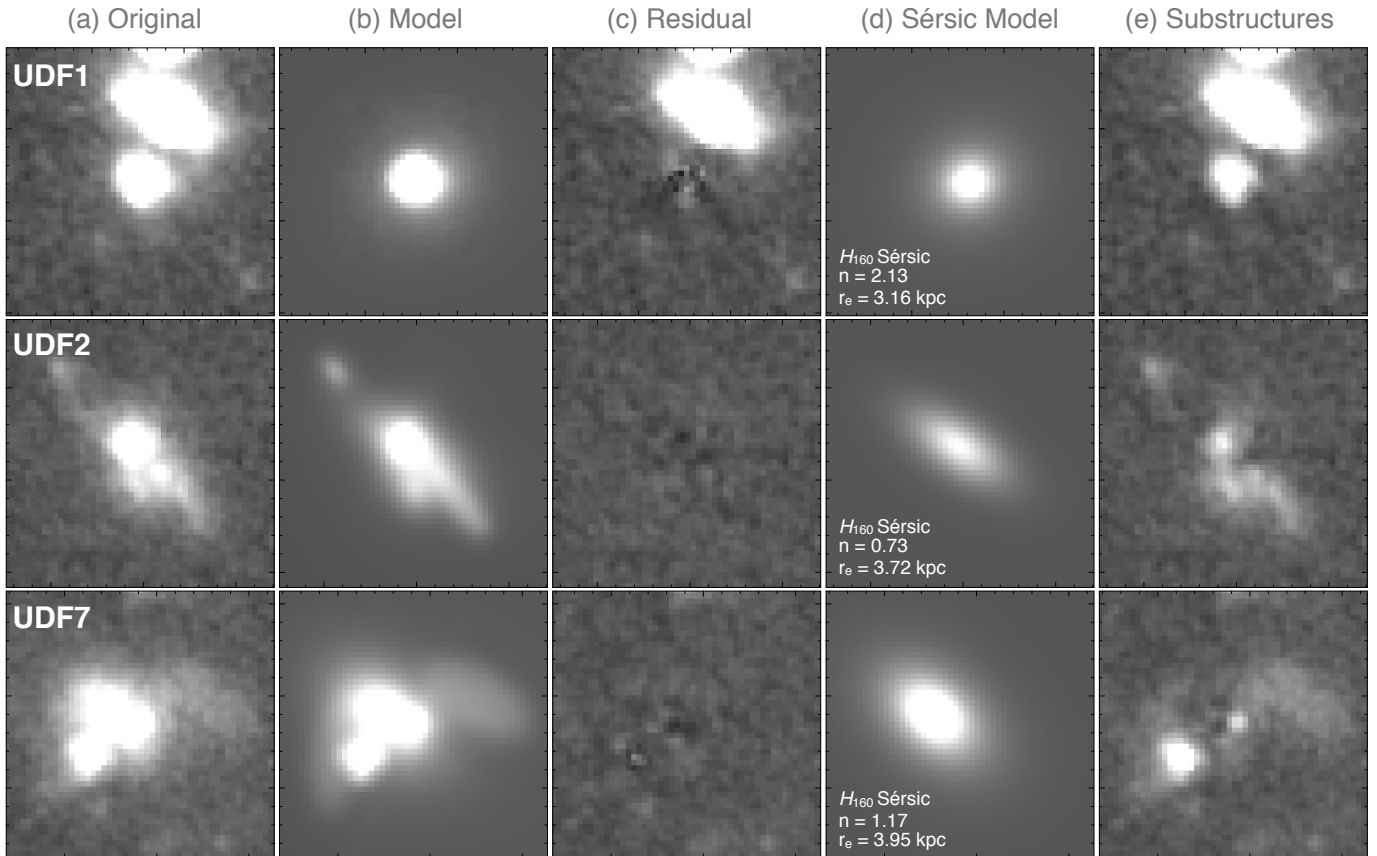


FIG. A1.— Steps taken to search for stellar mass substructures in the *HST*  $H_{160}$  observations, which probe the rest-frame optical emission. Briefly, we model all emission components (column b) to achieve a uniform residual (column c), then only subtract the dominant Sérsic model (column d) to produce substructure maps (column e).